Winter mixing preconditioning of the spring phytoplankton bloom in the Bay of Biscay

Authors: Ricardo González-Gil[1*], Fernando González Taboada[2,3], Carlos Cáceres[4], John L. Largier[5], Ricardo Anadón[1]

* Contact author e-mail: rgonzalezgil@gmail.com

1. Área de Ecología, Dpto. Biología de Organismos y Sistemas, Universidad de Oviedo, C/Valentín Andrés Álvarez s/n, E33071 Oviedo, Asturias, Spain.

2. Princeton University, Princeton, NJ 08540 USA.

3. Geophysical Fluid Dynamics Laboratory, National Oceanic and Atmospheric Administration, Princeton, NJ 08540 USA.

4. Dept. of Mathematics and Statistics, University of Strathclyde, 26 Richmond St, Glasgow G1 1XQ, UK

5. Bodega Marine Laboratory, University of California, Davis, 2099 Westside Drive, Bodega Bay, CA 94923-0247 USA.

Running head: Winter mixing and spring bloom

Key words: winter mixing, spring phytoplankton bloom, time series, global warming, remote sensing, Bay of Biscay

Abstract

The spring phytoplankton bloom plays a key role in the dynamics of temperate and polar seas. Nevertheless, the mechanisms and processes behind these blooms remain a subject of considerable debate. We analyzed the influence of deep mixing during winter on the spring phytoplankton bloom in the Cantabrian Sea (southern Bay of Biscay). To this end, we combined long-term physical and biogeochemical in situ data (1993-2012) and satellite observations (1997-2012). Deeper winter mixing led to higher nitrate and chlorophyll concentrations through the water column during the spring bloom. However, this effect was modified by short time-scale variability in near-surface stratification in spring. Winter mixing preconditioning also influenced different spring bloom metrics: deeper and later mixing in winter was followed by later blooms with a larger peak. In these enhanced blooms, nitrate was taken up at faster rates, indicating higher rates of phytoplankton production. Winters with weaker mixing (that led to weaker spring blooms) were associated with warmer surface temperatures. This relationship suggests that the multi-decadal trend towards warmer surface temperatures in the Bay of Biscay may promote a decrease in the magnitude of the spring bloom, which could impact upper trophic levels and also deep carbon export in the future.

Introduction

Every year, the spring phytoplankton bloom reappears in temperate and polar seas, turning surface waters green. This phenomenon has fascinated researchers since the early days of oceanography in the 19th century (Banse 1992; Fischer et al. 2014). In the last decades, satellite images of surface chlorophyll concentration led to a renewed interest in phytoplankton blooms by revealing their ubiquity and large spatial extent (Parsons and Lalli 1988; Yoder et al. 1993; McClain 2009). Vernal phytoplankton blooms drive the pumping of important amounts of atmospheric carbon into deep oceanic waters, making them a key component of biogeochemical cycles (Longhurst and Harrison 1989; Falkowski et al. 1998; Sarmiento and Gruber 2006). At the same time, these blooms support a large proportion of the annual productivity of higher trophic levels, including many exploited species (Hjort 1914; Cushing 1990; Townsend et al. 1994).

The North Atlantic spring phytoplankton bloom stands out as the most pronounced bloom in open ocean waters (Yoder et al. 1993), although its characteristics vary substantially in space and time (Ueyama and Monger 2005; Racault et al. 2012; González Taboada and Anadón 2014). Interannual changes in the timing and magnitude of phytoplankton blooms can lead to a trophic match-mismatch that modulates the survival of upper trophic levels, including commercially fished stocks (Cushing 1990; Platt et al. 2003; Durant et al. 2007; Koeller et al. 2009; Kristiansen et al. 2011). With such important impacts, there is a growing interest in understanding the factors that promote interannual variability in the characteristics of the spring phytoplankton bloom, especially in the context of global climate change (Racault et al. 2012). Different hypotheses have been proposed to explain the mechanisms that trigger the onset of

spring blooms, leading to an intense and ongoing debate (Behrenfeld and Boss 2014; Lindemann and St. John 2014; Chiswell et al. 2015; Ferreira et al. 2015). Most of the drivers involved in these mechanisms also influence the magnitude of the bloom (Follows and Dutkiewicz 2002; Henson et al. 2006; Henson et al. 2009).

Among the physical processes that influence bloom development, deep mixing in winter stands out due to its crucial role in preconditioning the environment for a phytoplankton bloom in the next spring. During winter, deep convective mixing leads to the replenishment of near-surface nutrients (Williams and Follows 2003). Inorganic nitrogen compounds, such as nitrate, are usually among the most limiting for phytoplankton productivity (Falkowski et al. 1998; Moore et al. 2013) and thus, their availability is an important factor controlling the development of spring blooms (see for example Sambrotto et al. 1986; Sieracki et al. 1993; D'Ortenzio et al. 2014). As winter progresses towards spring, nutrients in surface layers become suddenly isolated from deeper waters with the onset of seasonal stratification. This sets an upper bound on the amount of nutrients available for phytoplankton in spring because, for many species, the access to nutrients below the seasonal thermocline is very limited. Deep mixing also constrains phytoplankton growth and the density of seeding populations by reducing the residence time of individual phytoplankters in the euphotic layer (Sverdrup 1953), although it simultaneously decreases encounter rates with grazers due to dilution effects (Yoshie et al. 2003; Behrenfeld 2010; Behrenfeld and Boss 2014).

With such a variety of effects operating together, the question that arises is: how and to what extent does winter mixing influence the spring phytoplankton bloom? Several studies have investigated the role of winter mixing in determining the magnitude of spring blooms (e.g. Follows and Dutkiewicz 2002; Henson et al. 2009; Martinez et al.

2011), but we are not aware of any analyses of how winter mixing affects other characteristics such as bloom timing and duration. In addition, phytoplankton blooms are usually analyzed either in terms of changes in surface or in depth-integrated chlorophyll, ignoring potential changes in vertical structure (Chiswell et al. 2015). Indeed, phytoplankton community structure varies consistently across vertical gradients in the water column, with marked changes in physiological, ecological and taxonomic patterns (Reynolds 2006).

A proper characterization of spring phytoplankton blooms demands high frequency sampling to cope with rapid changes in phytoplankton biomass (Rantajärvi et al. 1998). This imposes a major constraint on analyses of change in phytoplankton phenology. The availability of daily satellite ocean color measurements only partially alleviates this problem, given the lack of data during cloudy periods and the limitation of measurements to surface waters (McClain 2009). On the other hand, traditional approaches based on in situ sampling allow the collection of information at different depths, but sustained sampling based on recurrent oceanographic cruises spanning many years is limited to lower frequency sampling (Karl 2010; Church et al. 2013).

We combined long-term, monthly, in situ data (1993-2012) with quasi-daily satellite observations (1997-2012) to analyze the influence of deep winter mixing on the spring phytoplankton bloom in the central Cantabrian Sea, southern Bay of Biscay. In this temperate sea, nutrient supply to upper layers is largely driven by deep mixing processes during winter (Llope et al. 2007; Hartman et al. 2013), leading to a well-developed spring bloom that is a major feature of the seasonal cycle of phytoplankton (Varela 1996). First, we examined the relationship of winter mixing with nitrate and phytoplankton concentrations through the water column during the spring bloom,

considering also short-term variability in the stability of the upper layer. Next, we assessed how inter-annual changes in winter mixing modulate the timing, duration and intensity of the surface expression of the spring bloom. Finally, we explored how changes in surface temperature impacts the development of the spring phytoplankton bloom through its influence on winter mixing. Through these analyses, we assess the relative importance of winter mixing on the interannual variability of the spring phytoplankton bloom in temperate seas.

115 ## Material and methods

116 The central Cantabrian Sea (southern Bay of Biscay, Fig. 1) has been sampled
117 intensively during the last two decades as part of the Spanish long-term monitoring
118 network RADIALES (www.seriestemporales-ieo.com, Valdés et al. 2002; Valdés et al.
119 2007). Here, we used samples collected monthly between 1993 and 2012 at station E3,
120 the most oceanic station of the Cudillero transect. Station E3 is located close to the shelf
121 break, but over the Avilés Canyon (06º10'W, 43º46'N, depth 870 m), and it reflects
122 oceanic conditions typical of a temperate sea. A detailed description of the station and
123 information about the protocols used can be found in Llope *et al.* (2006). We combined
124 these in situ samples with daily satellite data for surface chlorophyll *a* concentration
125 ([Chl *a*]$_{SAT}$) and sea surface temperature (SST) averaged over a 0.25º quadrangular
126 pixel centered at 6.125ºW and 43.875ºN (Fig. 1).

127 ### In situ oceanographic observations

128 We used 500-m CTD profiles (SeaBird-25) to assess the intensity of winter mixing
129 between 1993 and 2012. We estimated mixed layer depth (hereafter $MLD_{0.5}$) as the
130 depth where the temperature decreases 0.5ºC with respect to the temperature at 10 m
131 depth (Monterey and Levitus 1997). Then, we determined annual maximum winter
132 mixing depths (WMD_{max}) from $MLD_{0.5}$ estimates in winter months (January, February
133 or March), before the spring [Chl *a*]$_{SAT}$ maximum (see *Statistical analysis and spring*
134 *bloom metrics* section). Incomplete profiles or those showing a thermal inversion were
135 rejected to avoid under- or over-estimating $MLD_{0.5}$, respectively. Thermal inversions
136 were identified in profiles where temperatures exceeded the 10-m-depth temperature by
137 0.1°C or more over at least 25 m. It is important to note that, due to the monthly

sampling frequency, the deep mixing process leading to the measured WMD_{max} could have occurred days or weeks before the monthly sampling date, or that later events could lead to deeper mixing before sampling the next profile.

Short-term changes in near-surface stratification can mask the influence of winter mixing on spring bloom characteristics. To control for this masking effect, we included the estimated depth of near-surface stratification in our analysis. We estimated the depth of the near-surface stratification (hereafter $MLD_{0.1}$) on each sampling date from the depth at which temperature is 0.1ºC lower than at 4 m depth (or at 6 m depth, if 4 m was missing; see Dever et al. 2006; Chiswell 2011; Houpert et al. 2015). Daily variations in the near-surface stratification depth affect phytoplankton vertical distribution and the local conditions experienced by phytoplankton cells during the spring bloom (Chiswell 2011; Chiswell et al. 2015; Franks 2015). Heating of surface water is the primary source of stratification, which suppresses near-surface turbulence (Franks 2015). Therefore, the depth of thermal stratification largely controls how far phytoplankton cells can be moved away from the surface and thus determines the amount of light received by phytoplankton.

We examined changes in observed nitrate and chlorophyll *a* (Chl *a*) concentrations in the upper 200 m to analyze the potential bottom-up effects of winter mixing on spring phytoplankton blooms. Nitrate is the most limiting nutrient of phytoplankton growth in the area (Llope et al. 2007), while Chl *a* data were used as a proxy for phytoplankton biomass. Both nitrate and Chl *a* samples were collected at eight depths (~ 0, 10, 20, 30, 40, 50, 75, 100, 150, 200 m) at station E3 using 5-L Niskin bottles. Nitrate samples were frozen and stored at -20ºC before measuring nitrate concentrations using a Technicon AAII Autoanalyser (Industrial Method 158-71 W/A) and a Skalar SANplus

(Skalar Analytical B.V.). Post-cruise nitrate concentrations were converted from μmol L^{-1} to μmol kg^{-1} using water density estimates at average laboratory conditions (22.5ºC and 98.6 kPa at 232 m.a.s.l.). Chl *a* concentrations were estimated by filtering samples through GF-F filters (25 mm diameter), using 200 mL for low-Chl *a* samples, and 100 mL for high-Chl *a* samples. These filters were subsequently frozen at -20ºC. Then, Chl *a* was extracted in 10 mL of 90% acetone during 24 h in darkness at 4ºC. Chl *a* concentrations were measured using a Turner Designs 10 fluorometer following the method of Yentsch and Menzel (1963).

We explored seasonal and interannual variability in Chl *a* and nitrate concentrations through the water column using contour plots based on kriging interpolation (Nychka et al. 2015). Before kriging, we used linear interpolation to ensure that the shape of vertical profiles was locally preserved in the contour plots (i.e. by estimating concentrations every two meters). We also used linear interpolation to estimate missing Chl *a* and nitrate concentrations in the profile of a given date before calculating depth-integrated values. Linear interpolation was preceded by a $\log_{10}$ transformation of Chl *a* concentrations. To avoid unreliable estimates, we discarded profiles containing only one data point. We calculated depth-integrated Chl *a* and nitrate using the trapezoidal rule. Depth-integrated Chl *a* was calculated for ~0 to 200 m depth and regarded as a proxy of total phytoplankton biomass in the water column. Nitrate was integrated from ~ 0 to 50 m depth, just below the nitracline depth during the seasonal stratification (see Figs. 2 and 3). Nitrate in this upper layer is extensively exploited by phytoplankton during the spring bloom. The nitracline was defined by a threshold concentration of 1 μmol kg^{-1}, following Cullen and Eppley (1981).

185 **Remote sensing data**

186 We used a time series of remotely sensed surface Chl *a* concentration ([Chl *a*]$_{SAT}$) to
187 characterize the development of the spring phytoplankton bloom. In temperate latitudes,
188 [Chl *a*]$_{SAT}$ provides a reliable proxy of phytoplankton biomass (McClain 2009). Satellite
189 retrievals were averaged over a 0.25 x 0.25º quadrangle covering station E3 (Fig. 1).
190 Daily time series of [Chl *a*]$_{SAT}$ between September 1997 and December 2012 were
191 retrieved from Level 3 (geolocated, corrected and averaged over a regular grid)
192 SeaWiFS (Sept. 1997-Dec. 2007, reprocessing R2010.0) and Aqua MODIS (Jul. 2002-
193 Dec. 2012, reprocessing R2013.1.1) standard mapped images (SMI) available at the
194 Ocean Color Web (NASA OBPG 2015a; b). Estimates of [Chl *a*]$_{SAT}$ were derived using
195 version six of the OC4 (SeaWiFS) and OC3M (Aqua MODIS) empirical band-ratio
196 algorithms (O'Reilly et al. 2000, oceancolor.gsfc.nasa.gov/cms/atbd/chlor_a).

197 We also used remotely sensed sea surface temperature (SST, see *Statistical analysis*
198 *and spring bloom metrics* section). The SST time series (from September 1981 to
199 December 2012) was derived from the NOAA-Optimum Interpolation 1/4 Degree Daily
200 Sea Surface Temperature Analysis (OISST version 2). The methods are described in
201 Reynolds et al. (2007). The database of SST images is produced and maintained by C.
202 Liu and R. W. Reynolds at NCDC (www.ncdc.noaa.gov/oisst). SST is one of the most
203 important parameters in the dynamics of pelagic ecosystems: it has a direct effect on
204 metabolic rates (Eppley 1972; Ikeda 1985), and it is an indicator of many physical
205 processes that affect pelagic organisms, such as mixing and upwelling. Thus, we also
206 explored the relationship between SST and the intensity of mixing in winter.

Statistical analysis and spring bloom metrics

The characterization of the spring phytoplankton bloom and the influence of winter mixing differed depending on whether in situ data or remotely sensed data were used. In the case of in situ sampling, the availability of data through the entire column allowed us to study variations in the development of the bloom at different depths, considering also concomitant changes in nitrate concentration. On the other hand, higher frequency satellite data allowed extraction of different bloom metrics, although this approach was restricted to surface waters. To conduct our analyses, we combined simple linear regressions and Generalized Additive Models (GAMs, Hastie and Tibshirani 1990). The main characteristic of GAMs is the inclusion of unspecified smooth functions to capture nonlinear relationships among the response and predictor variables (see *Supporting information* for further details). We assumed independent and identically distributed normal errors in all cases, which required $\log_{10}$ transformation of Chl *a* data before the analyses (both in situ and satellite). Nevertheless, model assumptions were checked by examining the distribution of residuals. All the statistical analyses were performed in R version 3.3.3 (R Core Team 2017) using RStudio interface version 1.0.143 (RStudio Team 2016). GAMs were fitted using the functions gam and t2 from the package mgcv (v1.8-17, Wood 2006; Wood et al. 2013). We also used the package LatticeKrig v6.2 (Nychka et al. 2016) for kriging interpolation. Figures were created using package ggplot2 (v2.2.1, Wickham 2009) and graphically improved in Inkscape (www.inkscape.org).

228 Characterization of seasonality

229 We characterized the shape of the seasonal cycle for physical variables (SST, $MLD_{0.5}$
230 and $MLD_{0.1}$), nitrate and Chl *a*. We fitted the following GAM to each physical variable,
231 depth-integrated nitrate and Chl *a*, surface nitrate concentration and $[\text{Chl } a]_{SAT}$ (all of
232 them represented below as y):

$$y = a + f(t) + \varepsilon \quad (1)$$

233 The model includes an intercept (a), a 1D smooth function (f) to compute the seasonal
234 curve over the day of the year (t) and an error term represented by ε (see *Supporting*
235 *information* for further specifications).

236 In the case of in situ Chl *a* and nitrate concentration, we estimated the seasonality
237 through the water column using a GAM that included an interaction term between the
238 day of the year (t) and depth (z):

$$y = a + te(t, z) + \varepsilon \quad (2)$$

239 where the interaction term $te(t, z)$ is a 2D smooth function (specifically, a tensor
240 product, te) that captures the seasonal cycle of the vertical profiles of Chl *a* and nitrate
241 concentration over the day of the year (Wood 2006).

242 Analysis of the winter mixing effect based on in situ data

243 We first inspected the effect of deep mixing on depth-integrated nitrate in winter
244 using a simple linear regression. Then, to examine the influence of winter mixing on

spring-bloom Chl *a* and nitrate concentrations through the water column, we identified the month with maximum surface Chl *a* concentration during the first half of each year. We considered this month as representative of conditions during the spring bloom. We formulated then a set of alternative models to explore the influence of WMD_{max} and $MLD_{0.1}$ on vertical profiles of Chl *a* and nitrate that month (see Table 1). Alternative models were later compared based on Akaike Information Criterion (AIC, Burnham and Anderson 2002). The basic null model, which only included an intercept, was expanded by adding terms for the influence of depth and for the interaction effect between depth and either WMD_{max} or $MLD_{0.1}$ (note that WMD_{max} and $MLD_{0.1}$ were uncorrelated, r = 0.11, p-value = 0.688). These interaction terms were included to capture a distinct depth-dependent effect of WMD_{max} or $MLD_{0.1}$. We completed the analysis by testing the existence of an interaction effect between WMD_{max} and $MLD_{0.1}$, although we limited this analysis to surface waters (See Table 2 for the list of models tested). This enabled an easier comparison with satellite information. Additionally, we explored this interaction effect for depth-integrated Chl *a*.

We concluded the analysis of profile data by examining the impact of winter mixing on new primary production (PP_{new}) during the spring bloom. Assuming that the effect of transport and external sources is negligible, we can ascribe the drawdown of nitrate in the upper layers mainly to phytoplankton uptake. This provides a rough approximation of PP_{new} (mg C m^{-2} day^{-1}) during the bloom:

$$PP_{new} \sim f_{C:N} \int_{50}^{0} \frac{1}{\Delta t} \left([\mathrm{NO_3}]_{z,t_i} - [\mathrm{NO_3}]_{z,t_f} \right) \mathrm{d}z \qquad (3)$$

where the decay in nitrate concentration $[NO_3]$ at depth z (mol m^{-3}) between February (t_i) and April (t_f) was integrated over the upper 50 m of the water column (i.e. from just below the nitracline depth during the seasonal stratification, see Figs. 2 and 3). For each season, we subtracted nitrate concentrations in February from those recorded in April to cover the entire bloom development. Differences in $[NO_3]$ were averaged over time (days) using the difference among sampling dates, Δt. The factor used in the conversion from nitrate to carbon units ($f_{C:N}$) was based on a constant C:N ratio ($r_{C:N} = 6.6$) averaged from the C:N ratios for the new production estimated by Körtzinger et al. (2001) in bloom and early bloom sampling stations during a meridional transect carried out in the Northeast Atlantic. This $r_{C:N}$ coincides with the ratio described by Redfield (1958) for the particulate organic matter in the ocean. We calculated PP_{new} for each season and compared it with the intensity of winter mixing using a simple linear regression on WMD_{max} measured during the preceding winter. We presumed that a positive relationship between PP_{new} and WMD_{max} would be indicative of the preconditioning effect of winter mixing on the spring bloom development.

Spring bloom characterization based on satellite data

The high temporal resolution of satellite data on [Chl a]$_{SAT}$ allowed us to extend the analysis of interannual variability in the spring bloom. To do that, we fitted a GAM featuring a changing seasonal cycle among years both to [Chl a]$_{SAT}$ and SST data (y):

$$y = a + f(t|year) + \varepsilon \quad (4)$$

where a corresponds to the intercept, t to the day of the year, and ε is an error term. The $f(t|year)$ term is included to capture changes in the seasonality among years. In

the model, the seasonal cycle starts in July 15th (or 14th in a leap year). This choice ensured that the seasonal term included the annual SST maximum and next year SST minimum, both required to derive spring bloom metrics (see below). For [Chl *a*]$_{SAT}$, analyses conducted beforehand indicated that there is no need to account for differences in mean concentration or in the shape of the seasonal cycle between sensors (SeaWiFS and Aqua MODIS). Lack of [Chl *a*]$_{SAT}$ information during the period 1997-1998 resulted on unreliable estimates of bloom metrics that were not included in the main analyses.

We retrieved a series of metrics to characterize interannual changes in the spring bloom based on modelled time series of [Chl *a*]$_{SAT}$ (Eq. 4). We determined first the timing of the autumn bloom, which follows the annual SST maximum. The autumn bloom was defined as the first local maximum in [Chl *a*]$_{SAT}$ reached after at least 30 consecutive days of increase in [Chl *a*]$_{SAT}$ (this condition prevents confounding this bloom with a small rise in [Chl *a*]$_{SAT}$). Then, we defined spring *bloom rise* as the day when the seasonal curve of [Chl *a*]$_{SAT}$ increased at the fastest rate following the autumn bloom. If no autumn bloom was observed (i.e. only one [Chl *a*]$_{SAT}$ maximum occurred), then spring *bloom rise* was defined as the date when the [Chl *a*]$_{SAT}$ seasonal curve increased at the fastest rate. This criterion to identify the timing of the spring bloom avoids the use of an a priori chlorophyll threshold (for references discussing different criteria, see Brody et al. 2013; Blondeau-Patissier et al. 2014; González Taboada and Anadón 2014). We defined *bloom decay* as the day when the [Chl *a*]$_{SAT}$ seasonal curve decreased at the fastest rate after both the spring bloom maximum (i.e. the magnitude of the spring bloom peak, *max Chl a*) and minimum SST. The latest condition aimed to identify the real decay of the spring bloom, avoiding a confusion with an early,

310 temporary decrease in [Chl *a*]$_{SAT}$ after reaching the *max Chl a*. The day of occurrence of
311 the *max Chl a* was another timing metric (*max Chl a day*). Finally, we identified the
312 *bloom span* as the number of days between *bloom rise* and *bloom decay*.

313 Once we calculated these bloom metrics for each year, we inspected the influence of
314 winter mixing on them by using simple linear regression analysis. We also used linear
315 regressions to analyze SST long-term trends and to explore the impact of SST on the
316 magnitude of winter mixing at different lags.

317

Results

Seasonality

Physical variables (SST, $MLD_{0.5}$, $MLD_{0.1}$) and both nitrate and Chl *a* concentrations at different depths, or integrated through the water column, all showed a clear seasonal pattern (Figs. 2 and 3). The seasonal amplitude of SST ranged from an average maximum of 20.34ºC in August to an average minimum of 12.54ºC in March (Fig. 3a). In mid-winter (January and February), both $MLD_{0.5}$ and $MLD_{0.1}$ were deep, indicating a well-mixed water column (Fig. 3b). Some profiles showed shallower $MLD_{0.1}$ than $MLD_{0.5}$ during the well-mixed period. This decoupling probably indicates that the past mixing events leading to the measured $MLD_{0.5}$ might have occurred days or even weeks before the corresponding sampling dates, providing enough time for some stratification to develop. As a consequence of the mixing, nitrate was homogeneously distributed through the water column (average concentration of 4.68 μmol kg^{-1}, Fig. 3c), showing a seasonal peak in upper layers (Figs. 3c, 3e and 3g). At the end of February, a surface stratified layer was forming (shallow $MLD_{0.1}$) – the beginning of seasonal stratification (Fig. 3b). Concurrently, surface nitrate started to decrease and remained very low during the stratification period, from May to October (mean concentration in the top 20 m of 0.28 μmol kg^{-1}), causing the formation of a nitracline at a depth of ~ 40 m (Figs. 2a and 3c).

In contrast to nitrate, Chl *a* exhibited higher concentrations in near-surface waters except in mid-winter, when mixing homogenized the water column (Fig. 3d). Depth-integrated Chl *a* increased markedly in late December (Fig. 3f), although this increase was not noticeable in surface waters until late February (Figs. 3d and 3h). This fast

increase in Chl *a* corresponds to the spring bloom and leads to the seasonal nitrate depletion and the annual maximum in phytoplankton biomass, which generally occurred in March near the surface (Figs. 3d, 3h and 4) and ranged from 0.23 to 5.41 mg m^{-3} (average Chl *a* concentration in the uppermost 20 m). The annual maximum decreased in magnitude with depth and occurred later at intermediate-depth waters from 30 to 50 m (Fig. 4). From June to September, Chl *a* concentrations remained low near the surface (Figs. 3d and 3h) and were maximum between 20 and 50 m (0.33 mg m^{-3} on average). Surface Chl *a* concentration increased again during the autumn bloom, which was usually weaker than the spring bloom (average Chl *a* concentration of 0.18-2.64 mg m^{-3} in the uppermost 20 m).

Effect of WMD_{max} on the vertical structure of the spring bloom

Maximum winter mixing depths (WMD_{max}) exhibited inter-annual variability in both magnitude and timing (Fig. 5a). This variability affected the nutrient supply to surface layers: the deeper the WMD_{max}, the larger the depth-integrated nitrate over the upper 50 m layer at the WMD_{max} sampling date (Figs. 5b and 5c). Winter mixing also has an effect on nitrate levels and Chl *a* in spring blooms, as seen in Table 1 where model results are shown. Data for March were used for these analyses, the month in which the near-surface spring bloom typically peaks (Figs. 3d, 3h and 4). The model that includes WMD_{max} and $MLD_{0.1}$ as predictors of nitrate and Chl *a* concentrations performed best (Table 1). This indicates that both the past and recent history of the physical structure of the water column (i.e. WMD_{max} and $MLD_{0.1}$, respectively) have an effect on nitrate and Chl *a* concentration during the spring bloom. This model shows that higher nitrate and Chl *a* concentrations in March follow winters with deeper WMD_{max} (left panels in Fig. 6). The positive effect of WMD_{max} on nitrate concentration was more important towards

365 the surface (i.e. the increase in the effect along the x axis is gradually larger towards
366 shallower depths in the left panel of Fig. 6a). A similar effect was found for Chl *a*; the
367 positive effect of WMD_{max} was also strongest in surface waters and it became weaker at
368 deeper depths, especially at intermediate layers (left panel in Fig. 6b). In both cases, the
369 near-surface seasonal depletion of nutrients during stratification (Figs. 3c, 3e and 3g)
370 can explain the higher near-surface sensitivity of nitrate and Chl *a* to winter mixing.

371 Contrary to the effect of WMD_{max}, the relationship between near-surface
372 stratification depth ($MLD_{0.1}$) and either nitrate or Chl *a* concentrations in March varied
373 markedly across depth (right panels in Fig. 6). In the case of nitrate, near-surface
374 concentrations decrease when $MLD_{0.1}$ is shallow ($MLD_{0.1}$ ~ 0 to 75 m, right panel of
375 Fig. 6a), with strongest decreases for shallowest $MLD_{0.1}$. This effect of $MLD_{0.1}$ on
376 nitrate is consistent with rapid nutrient drawdown when phytoplankton blooms are
377 confined within a thin surface layer. Consistent with this forcing, large Chl *a*
378 concentrations are seen near-surface and at depth (below ~ 150 m) when $MLD_{0.1}$ is less
379 than ~100 m (see right panel of Fig. 6b). The effect in other sections of the water
380 column (below ~ 50 m for nitrate, but ~ 30-150 m for Chl *a*) peaked at intermediate
381 $MLD_{0.1}$ (~ 50-125 m).

382 Table 2 summarizes the effect of WMD_{max} and $MLD_{0.1}$ on nitrate and Chl *a*
383 concentrations at the surface (~ 0 m depth) in March. In the case of nitrate, the model
384 including only the $MLD_{0.1}$ explained around three times more variability than the
385 WMD_{max} alone (Table 2); the model including an interaction showed a similar positive
386 effect of $MLD_{0.1}$ along the entire WMD_{max} range, but a decreasing positive effect of
387 WMD_{max} towards deeper $MLD_{0.1}$ (Fig. 7a). In the case of Chl *a*, the interaction model
388 outcompeted the others (Table 2). For the analysis of the model outputs portrayed in

389 Fig. 7b, we focused on those regions of the sample space with observations. Surface Chl
390 *a* concentration was maximum for deep WMD_{max}-shallow $MLD_{0.1}$ and showed a
391 secondary maximum for ~ 50-100 m $MLD_{0.1}$. Depth-integrated Chl *a* in March, which
392 was highly correlated with Chl *a* at 20-30 m depth (*Supporting information* Fig. S1a),
393 showed a similar response pattern as surface Chl *a*. However, in this case, the estimated
394 maximum depth-integrated Chl *a* showed for deep WMD_{max}-shallow $MLD_{0.1}$ and
395 intermediate-deep $MLD_{0.1}$ (~ 50-150 m) approximately the same values (Fig. S1b).

396 The new primary production (PP_{new}) during the spring bloom, estimated from depth-
397 integrated nitrate (0-50 m) depletion, ranged between 30 and 490 mg C m^{-2} day^{-1} (Fig.
398 8). We found a clear relationship among primary production and mixing during the
399 previous winter (R^2 = 0.41, p-value < 0.050). Our linear regression model predicts an
400 increase in PP_{new} of ~ 64 mg C m^{-2} day^{-1} for every 100 m of increase in WMD_{max}. We
401 discarded the possibility that this result was promoted by a spurious correlation between
402 WMD_{max} and the number of days between sampling dates (r = -0.09, p-value > 0.700).

Effect of WMD_{max} on spring bloom metrics

High resolution satellite data allowed characterization of the development of the spring phytoplankton bloom in the surface. Spring bloom phenology presented a high interannual variability (Fig. 9), spanning an average of ~ 90 days and peaking usually between March and April (mean date, April 4th; range, February 17th to May 22nd). The magnitude of the bloom peak varied also between years, with [Chl *a*]$_{SAT}$ peak concentrations ranging from 0.53 to 1.43 mg m^{-3}. Changes in bloom magnitude were positively associated with WMD_{max} (Fig. 10e), as expected from the analysis of in situ data. Later blooms with a shorter span followed winters with deeper mixing layers (Figs. 10a and 10i), although the effect of WMD_{max} on these timing metrics remained more elusive (R^2 = 0.15, p-value = 0.165 and R^2 = 0.18, p-value = 0.133 for bloom rise and bloom span, respectively). As mentioned above, the bloom was more productive in these years (Fig. 8). Additionally, the later the WMD_{max} occurred, the later the spring bloom peaked (Fig. 10h). A simple linear correlation analysis showed that WMD_{max} and the WMD_{max} sampling day were uncorrelated (r = 0.30, p-value = 0.302).

Impact of SST on WMD_{max}

The WMD_{max} was negatively correlated with the SST at different day lags, indicating that shallower WMD_{max} follow warmer SST (Fig. 11a). These negative relationships were stronger for the SST within the ~ 60 days previous to the winter mixing event; this implies that, as most WMD_{max} occurred in February and March (Fig. 5a), the December-March SST has the strongest impact on winter mixing. On the other hand, the SST seasonal cycle presented large inter-annual variations in the study area (Fig. 9). Beyond the observed linear trend (0.30 ºC decade^{-1}, 1981-2012), these changes reflect

426 different rates of warming through the year, with largest values observed during the
427 period of seasonal stratification (spring to early autumn), when the trend frequently
428 exceeds 0.30 ºC decade^{-1} (Fig. 11b). Positive trends in SST, together with the mentioned
429 link between SST and WMD_{max}, entail a long-term decline in WMD_{max} and,
430 consequently, in the magnitude of the spring bloom peak (see Fig. 10e). However, the
431 short length of the record prevented a direct assessment of these trends and further
432 exploration of this link is required.

Discussion

Our results highlighted a strong winter mixing preconditioning of the development and characteristics of the spring phytoplankton bloom, modulated by the near-surface stratification. Deeper and later maximum winter mixing leads to more intense, later blooms. These more intense blooms were also likely more productive, as suggested by the larger decreasing rate of nitrate observed within the upper layers. Additionally, we found that higher winter SST is associated with weaker convective mixing in winter and thus also with weaker spring phytoplankton blooms.

The dynamics of the spring phytoplankton bloom remain a subject of active debate among marine scientists (see Behrenfeld and Boss 2014; Chiswell et al. 2015 for recent reviews). Some of this controversy arises from the adoption of different methods to characterize phytoplankton blooms (Ji et al. 2010), with contrasting findings depending on whether the analyses focused on surface or depth-integrated phytoplankton biomass (Chiswell et al. 2015). Nevertheless, both approaches disregard the depth-dependence of the phytoplankton response, which we describe here and that accounts for differences in timing and magnitude of the spring bloom.

The spring bloom exhibits yearly an apparent northward or southward progression in the Northern and Southern Hemisphere, respectively (Siegel et al. 2002; Henson et al. 2009; Chiswell et al. 2013). Analogously, in the Bay of Biscay and probably in other temperate regions (see for example Chiswell 2011), this bloom occurs asynchronously through the water column, showing each year an apparent development towards subsurface layers as spring progresses and the water column stratifies. For upper layers, this might mainly reflect differences among depths in the moment of optimal nutrient

456 and light conditions for phytoplankton growth (Klausmeier and Litchman 2001). In
457 deep layers, an advanced timing of maximum Chl *a* concentration might reflect both a
458 larger arrival of phytoplankton cells from surface waters and the contribution of
459 phytoplankton growth during winter, potentially due to a dilution effect on grazing
460 (Behrenfeld 2010; Behrenfeld 2014; Behrenfeld and Boss 2014). The observed steady
461 seasonal increase in depth-integrated phytoplankton biomass since early winter supports
462 this last aspect to some extent, with the reservations required as a consequence of
463 limited data availability during winter.

464 The estimated seasonal cycle of Chl *a* showed that the development and climax of
465 the spring bloom in surface waters take place around March in the Bay of Biscay. A
466 shift from a deep-mixing regime (primarily buoyancy-driven) to a low-turbulence
467 regime (mainly wind-driven) occurs during this critical period (Huisman et al. 1999;
468 Chiswell et al. 2013; Brody and Lozier 2014; 2015; Chiswell et al. 2015). This period
469 coincides also with the onset of the seasonal thermal stratification, triggered by a change
470 to positive air-sea heat fluxes (Chiswell 2011; Taylor and Ferrari 2011; Ferrari et al.
471 2015). At this time, nitrate conditions are largely controlled by the magnitude of
472 previous deep winter mixing events in the Bay of Biscay, as already shown by Hartman
473 et al. (2013). However, inter-annual changes in the characteristics of upper water
474 masses and different hydrographic processes (e.g. the Iberian Poleward Current, IPC)
475 can modulate the effect of winter mixing on nutrient preconditioning (Llope et al.
476 2007).

477 Winter convective mixing enhances nutrient concentrations directly through nutrient
478 entrainment from deep waters (Mann and Lazier 2006; Sarmiento and Gruber 2006).
479 Also, it reduces the time spent by phytoplankton in the euphotic layer, lowering

population growth rates (Sverdrup 1953), and diluting phytoplankton concentrations (Evans and Parslow 1985; Backhaus et al. 2003; D'Asaro 2008). Both processes would reduce nutrient uptake by phytoplankton in the upper ocean. However, this dilution effect might also reduce encounter rates with potential grazers, lowering the grazing pressure on phytoplankton population in winter (Yoshie et al. 2003; Behrenfeld 2010; Behrenfeld and Boss 2014). Combining the arguments presented above, deeper winter mixing can lead to a high nutrient-low grazing environment that may positively precondition phytoplankton growth during the spring bloom. Indeed, our analysis demonstrates that deeper winter mixing is associated with higher nutrient concentrations and more intense blooms also in the southern Bay of Biscay.

The physical structure of the water column during the spring bloom, characterized here by the extent of the surface stratified layer, plays also an important role in shaping the vertical distribution of phytoplankton (Chiswell 2011; Brody and Lozier 2015). The thickness of the stratified layer largely determines to which extent phytoplankton can be moved downward, away from maximum light intensities (Franks 2015). Shallow-intermediate surface stratified layers in March may keep phytoplankton close to the surface, leading to an increase in their growth rates (Chiswell 2011), and consequently enhance the biological removal of nitrate, especially in surface waters. Indeed, surface phytoplankton biomass was enhanced by shallow-intermediate stratified layers, especially after a favorable preconditioning by mid-large winter mixing events. At depth, higher Chl *a* concentrations during shallow-intermediate stratification and after mid-large winter mixing might reflect larger fluxes of sinking cells due to enhanced phytoplankton growth in the upper layers (Falkowski et al. 1998; Sanders et al. 2014). In temperate seas such as the Bay of Biscay, diatoms become the dominant

504 phytoplankton group during the spring bloom (Fernández and Bode 1994) and their
505 sinking rates can be greater than 100 m d^{-1}, enhanced by particle aggregation (Smayda
506 1970; Lampitt 1985; Smetacek 1985; Burd and Jackson 2009). Thus, increased diatom
507 growth in the surface during the bloom might lead to a rapid export of phytoplankton to
508 waters several hundreds of meters below. In the study area, this hypothesis is supported
509 by the large pulses of biogenic silica collected by deep sediment traps during the spring
510 blooms of 2012 and 2013 (Rumín-Caparrós et al. 2016; traps were moored at 1178 and
511 1154 m depth over the Avilés Canyon and westwards over the open slope, respectively).

512 Winter mixing preconditioning affected also different metrics of the spring bloom in
513 the surface layer. As observed in March for in situ Chl *a* concentrations, the high
514 nutrient environment caused by deeper winter mixing events was associated with larger
515 spring bloom peaks. The positive effects of deep convective mixing on the spring bloom
516 intensity has been observed in other areas of the North Atlantic (Martinez et al. 2011;
517 Behrenfeld et al. 2013). However, our results demonstrate that enhanced nitrate
518 concentrations following strong winter mixing also lead to a more rapid depletion of
519 nutrients in spring. This rapid consumption reflects a larger accumulation of
520 phytoplankton biomass and results in shorter but more intense blooms. In this way,
521 deeper mixing lead to higher community productivity in the Bay of Biscay (Hartman et
522 al. 2013) and larger peaks in spring zooplankton biomass and abundance (González-Gil
523 et al. 2015). This bottom-up perspective is also compatible with top-down mechanisms
524 raised in the context of the Dilution-Recoupling Hypothesis (Behrenfeld 2010). The
525 release of phytoplankton from grazing pressure in winters with enhanced mixing could
526 entail the development of a larger seeding population and a bloom of a greater
527 magnitude. Interestingly, a lower grazing rate could also reduce in situ nutrient

528 regeneration and foster nutrient consumption by enabling higher accumulations of
529 phytoplankton biomass (Banse 1992), with the overall result of more intense blooms
530 with a shortened span.

531 Strong surface cooling processes due to heat losses are one of the major drivers of
532 deep convective events in winter, as observed in 2005 in the Bay of Biscay (Somavilla
533 et al. 2009; Acuña et al. 2010; Somavilla Cabrillo et al. 2011). Also, intense winds
534 related to winter storms may contribute to stirring of the water column during deep
535 mixing (Henson et al. 2006). If any or both of these processes occur at the end of the
536 winter time, they could delay the beginning of the thermal stratification or break it
537 temporarily during its initial phase. The thermal stratification of the water column is
538 required for a full development of the surface spring bloom (Chiswell 2011; Chiswell et
539 al. 2015). Thus, later deep mixing events associated with lower atmospheric
540 temperatures and gales at the end of winter could delay the spring bloom climax
541 (Townsend et al. 1994; Henson et al. 2006; Álvarez et al. 2009). This could explain our
542 observation that later deep winter mixing events caused later spring bloom peaks.

543 The trend towards surface warming in the southern Bay of Biscay in winter is
544 consistent with both observational and model-based increases in heat content in North
545 Atlantic surface waters (Danabasoglu et al. 2012; Taboada and Anadón 2012). A larger
546 increase in surface heat content with respect to deeper layers entails larger energy inputs
547 to mix the water column (Levitus et al. 2012). The presumed decay in winter mixing
548 would cause a decline in the magnitude of the spring phytoplankton bloom in the
549 Central Cantabria Sea. Less intense blooms might decrease the strength of the biological
550 pump (Falkowski et al. 1998; Sanders et al. 2014), and they can also lead to a trophic
551 mismatch and a decrease in the production of upper trophic levels (Durant et al. 2007).

552 Nevertheless, the short length of the series analyzed in this study recommend caution
553 while interpreting trend results (e.g. Henson et al. 2010).

554 The impact of large-scale climate patterns such as the North Atlantic Oscillation
555 (NAO, Hurrell and Deser 2009) deters a simple interpretation of the long-term
556 variability in the Bay of Biscay. Indeed, changes in the intensity of winter mixing have
557 been linked to changes in atmospheric circulation and air-sea heat fluxes in the Bay of
558 Biscay associated with alternating phases of the NAO (Somavilla Cabrillo et al. 2011).
559 Positive NAO states promote surface warming and shallower mixing layers in winter.
560 However, it should be noted that extremely deep winter mixing events were common
561 following a decade long switch in NAO state starting in the mid-1990s. These strong
562 winter mixing events have been also associated with negative anomalies of the East
563 Atlantic (EA) pattern that bring cold, northerly winds into the southern Bay of Biscay
564 (Somavilla et al. 2009). Although continued warming might eventually conceal these
565 effects, the consequences of changes in winter mixing, spring stratification and the
566 interaction with long-term forcing remains elusive. Together, our findings recommend a
567 continued monitoring and further analysis of potential changes in plankton phenology in
568 the Bay of Biscay.

Conclusions

Deep winter mixing preconditioning affects nitrate and Chl *a* concentrations during the spring phytoplankton bloom in oceanic waters of the southern Bay of Biscay. Deeper winter mixing enhances phytoplankton biomass and nitrate concentrations during spring through the entire water column. At a shorter time-scale, the physical structure of the column, characterized by the extent of the surface stratified layer, had an important role in shaping the vertical profiles of nitrate and phytoplankton. Our results also show that deeper and later winter mixing events led to later and more intense spring blooms. The faster rate of nitrate uptake during this type of bloom suggests an enhanced production. Finally, we found that warm surface temperatures, especially in winter, were associated with weaker mixing of the water column and consequently, with a smaller spring bloom peak. Observations and predictions of increasing surface temperature in winter thus suggest a potential increase in the prevalence of smaller spring blooms and a reduction of upper trophic productivity and deep carbon export in the Bay of Biscay. This might also be observed in other temperate areas in the future.

584 **References**

585 Acuña, J. L., M. López-Alvarez, E. Nogueira, and F. González-Taboada. 2010. Diatom
586 flotation at the onset of the spring phytoplankton bloom: an *in situ* experiment.
587 Mar. Ecol. Prog. Ser. **400:** 115-125. doi:10.3354/meps08405

588 Álvarez, E., E. Nogueira, J. L. Acuña, M. López-Álvarez, and J. A. Sostres. 2009.
589 Short-term dynamics of late-winter phytoplankton blooms in a temperate
590 ecosystem (Central Cantabrian Sea, Southern Bay of Biscay). J. Plankton Res.
591 **31:** 601-617. doi:10.1093/plankt/fbp012

592 Backhaus, J. O., E. N. Hegseth, H. Wehde, X. Irigoien, K. Hatten, and K. Logemann.
593 2003. Convection and primary production in winter. Mar. Ecol. Prog. Ser. **251:**
594 1-14. doi:10.3354/meps251001

595 Banse, K. 1992. Grazing, temporal changes of phytoplankton concentrations, and the
596 microbial loop in the open sea, p. 409-440. *In* P. G. Falkowski and A. D.
597 Woodhead [eds.], Primary productivity and biogeochemical cycles in the sea.
598 Plenum Press.

599 Behrenfeld, M. J. 2010. Abandoning Sverdrup's critical depth hypothesis on
600 phytoplankton blooms. Ecology **91:** 977-989. doi:10.1890/09-1207.1

601 Behrenfeld, M. J. 2014. Climate-mediated dance of the plankton. Nat. Clim. Change **4:**
602 880-887. doi:10.1038/nclimate2349

603 Behrenfeld, M. J., and E. S. Boss. 2014. Resurrecting the ecological underpinnings of
604 ocean plankton blooms. Annu. Rev. Mar. Sci. **6:** 167-194. doi:10.1146/annurev-
605 marine-052913-021325

606 Behrenfeld, M. J., S. C. Doney, I. Lima, E. S. Boss, and D. A. Siegel. 2013. Annual
607 cycles of ecological disturbance and recovery underlying the subarctic Atlantic
608 spring plankton bloom. Glob. Biogeochem. Cycles **27:** 526-540.
609 doi:10.1002/gbc.20050

610 Blondeau-Patissier, D., J. F. R. Gower, A. G. Dekker, S. R. Phinn, and V. E. Brando.
611 2014. A review of ocean color remote sensing methods and statistical techniques
612 for the detection, mapping and analysis of phytoplankton blooms in coastal and
613 open oceans. Prog. Oceanogr. **123:** 123-144. doi:10.1016/j.pocean.2013.12.008

614 Brody, S. R., and M. S. Lozier. 2014. Changes in dominant mixing length scales as a
615 driver of subpolar phytoplankton bloom initiation in the North Atlantic.
616 Geophys. Res. Lett. **41:** 3197-3203. doi:10.1002/2014GL059707

617 Brody, S. R., and M. S. Lozier. 2015. Characterizing upper-ocean mixing and its effect
618 on the spring phytoplankton bloom with in situ data. ICES J. Mar. Sci. **72:** 1961-
619 1970. doi:10.1093/icesjms/fsv006

620 Brody, S. R., M. S. Lozier, and J. P. Dunne. 2013. A comparison of methods to
621 determine phytoplankton bloom initiation. J. Geophys. Res.: Oceans **118:** 2345-
622 2357. doi:10.1002/jgrc.20167

623 Burd, A. B., and G. A. Jackson. 2009. Particle aggregation. Annu. Rev. Mar. Sci. **1:** 65-
624 90. doi:10.1146/annurev.marine.010908.163904

625 Burnham, K. P., and D. R. Anderson. 2002. Model selection and multimodel inference:
626 a practical information-theoretic approach. Springer-Verlag.

627 Cullen, J., and R. Eppley. 1981. Chlorophyll maximum layers of the Southern
628 California Bight and possible mechanisms of their formation and maintenance.
629 Oceanol. Acta **4:** 23-32. http://archimer.ifremer.fr/doc/00121/23207/.

630 Cushing, D. 1990. Plankton production and year-class strength in fish populations: an
631 update of the match/mismatch hypothesis. Adv. Mar. Biol. **26:** 249-293.
632 doi:10.1016/S0065-2881(08)60202-3

633 Chiswell, S. M. 2011. Annual cycles and spring blooms in phytoplankton: don't
634 abandon Sverdrup completely. Mar. Ecol. Prog. Ser. **443:** 39-50.
635 doi:10.3354/meps09453

636 Chiswell, S. M., J. Bradford-Grieve, M. G. Hadfield, and S. C. Kennan. 2013.
637 Climatology of surface chlorophyll a, autumn-winter and spring blooms in the
638 southwest Pacific Ocean. J. Geophys. Res.: Oceans **118:** 1003-1018.
639 doi:10.1002/jgrc.20088

640 Chiswell, S. M., P. H. R. Calil, and P. W. Boyd. 2015. Spring blooms and annual cycles
641 of phytoplankton: a unified perspective. J. Plankton Res. **37:** 500-508.
642 doi:10.1093/plankt/fbv021

643 Church, M. J., M. W. Lomas, and F. Muller-Karger. 2013. Sea change: Charting the
644 course for biogeochemical ocean time-series research in a new millennium.
645 Deep Sea Res. Part II **93:** 2-15. doi:10.1016/j.dsr2.2013.01.035

646 D'Asaro, E. A. 2008. Convection and the seeding of the North Atlantic bloom. J. Mar.
647 Syst. **69:** 233-237. doi:10.1016/j.jmarsys.2005.08.005

648 D'Ortenzio, F. and others. 2014. Observing mixed layer depth, nitrate and chlorophyll
649 concentrations in the northwestern Mediterranean: A combined satellite and
650 NO3 profiling floats experiment. Geophys. Res. Lett. **41:** 6443-6451.
651 doi:10.1002/2014GL061020

652 Danabasoglu, G., S. C. Bates, B. P. Briegleb, S. R. Jayne, M. Jochum, W. G. Large, S.
653 Peacock, and S. G. Yeager. 2012. The CCSM4 ocean component. J. Clim. **25:**
654 1361-1389. doi:10.1175/JCLI-D-11-00091.1

655 Dever, E. P., C. E. Dorman, and J. L. Largier. 2006. Surface boundary-layer variability
656 off Northern California, USA, during upwelling. Deep Sea Res. Part II **53:**
657 2887-2905. doi:10.1016/j.dsr2.2006.09.001

Durant, J. M., D. Ø. Hjermann, G. Ottersen, and N. C. Stenseth. 2007. Climate and the match or mismatch between predator requirements and resource availability. Clim. Res. **33:** 271-283. doi:10.3354/cr033271

Eppley, R. W. 1972. Temperature and phytoplankton growth in the sea. Fish. Bull. **70:** 1063-1085.

Evans, G. T., and J. S. Parslow. 1985. A Model of Annual Plankton Cycles. Biological Oceanography **3:** 327-347. doi:10.1080/01965581.1985.10749478

Falkowski, P. G., R. T. Barber, and V. Smetacek. 1998. Biogeochemical controls and feedbacks on ocean primary production. Science **281:** 200-206. doi:10.1126/science.281.5374.200

Fernández, E., and A. Bode. 1994. Succession of phytoplankton assemblages in relation to the hydrography in the southern Bay of Biscay: a multivariate approach. Sci. Mar. **58:** 191-205. http://www.icm.csic.es/scimar/index.php/secId/196/IdArt/2688/.

Ferrari, R., S. T. Merrifield, and J. R. Taylor. 2015. Shutdown of convection triggers increase of surface chlorophyll. J. Mar. Syst. **147:** 116-122. doi:10.1016/j.jmarsys.2014.02.009

Ferreira, A. S. A., H. Hátún, F. Counillon, M. R. Payne, and A. W. Visser. 2015. Synoptic-scale analysis of mechanisms driving surface chlorophyll dynamics in the North Atlantic. Biogeosciences **12:** 3641-3653. doi:10.5194/bg-12-3641-2015

Fischer, A., E. Moberg, H. Alexander, E. Brownlee, K. Hunter-Cevera, K. Pitz, S. Rosengard, and H. Sosik. 2014. Sixty years of Sverdrup: a retrospective of progress in the study of phytoplankton blooms. Oceanography **27:** 222–235. doi:10.5670/oceanog.2014.26

Follows, M., and S. Dutkiewicz. 2002. Meteorological modulation of the North Atlantic spring bloom. Deep Sea Res. Part II **49:** 321-344. doi:10.1016/S0967-0645(01)00105-9

Franks, P. J. S. 2015. Has Sverdrup's critical depth hypothesis been tested? Mixed layers vs. turbulent layers. ICES J. Mar. Sci. **72:** 1897-1907. doi:10.1093/icesjms/fsu175

González-Gil, R., F. G. Taboada, J. Höfer, and R. Anadón. 2015. Winter mixing and coastal upwelling drive long-term changes in zooplankton in the Bay of Biscay (1993–2010). J. Plankton Res. **37:** 337-351. doi:10.1093/plankt/fbv001

González Taboada, F., and R. Anadón. 2014. Seasonality of North Atlantic phytoplankton from space: impact of environmental forcing on a changing phenology (1998–2012). Glob. Change Biol. **20:** 698-712. doi:10.1111/gcb.12352

696 Hartman, S. E., M. C. Hartman, D. J. Hydes, Z.-P. Jiang, D. Smythe-Wright, and C.
697 González-Pola. 2013. Seasonal and inter-annual variability in nutrient supply in
698 relation to mixing in the Bay of Biscay. Deep Sea Res. Part II **57:** 1303-1312.
699 doi:10.1016/j.dsr2.2013.09.032

700 Hastie, T. J., and R. J. Tibshirani. 1990. Generalized additive models. Chapman &
701 Hall/CRC.

702 Henson, S. A., J. P. Dunne, and J. L. Sarmiento. 2009. Decadal variability in North
703 Atlantic phytoplankton blooms. J. Geophys. Res.: Oceans **114:** C04013.
704 doi:10.1029/2008JC005139

705 Henson, S. A., I. Robinson, J. T. Allen, and J. J. Waniek. 2006. Effect of meteorological
706 conditions on interannual variability in timing and magnitude of the spring
707 bloom in the Irminger Basin, North Atlantic. Deep Sea Res. Part I **53:** 1601-
708 1615. doi:10.1016/j.dsr.2006.07.009

709 Henson, S. A., J. L. Sarmiento, J. P. Dunne, L. Bopp, I. Lima, S. C. Doney, J. John, and
710 C. Beaulieu. 2010. Detection of anthropogenic climate change in satellite
711 records of ocean chlorophyll and productivity. Biogeosciences **7:** 621-640.
712 doi:10.5194/bg-7-621-2010

713 Hjort, J. 1914. Fluctuations in the great fisheries of northern Europe viewed in the light
714 of biological research. Rapp. P.-V. Reún. Cons. Intern. Explor. Mer. **20:** 1-228.

715 Houpert, L., P. Testor, X. D. de Madron, S. Somot, F. D'Ortenzio, C. Estournel, and H.
716 Lavigne. 2015. Seasonal cycle of the mixed layer, the seasonal thermocline and
717 the upper-ocean heat storage rate in the Mediterranean Sea derived from
718 observations. Prog. Oceanogr. **132:** 333-352. doi:10.1016/j.pocean.2014.11.004

719 Huisman, J., P. van Oostveen, and F. J. Weissing. 1999. Critical depth and critical
720 turbulence: two different mechanisms for the development of phytoplankton
721 blooms. Limnol. Oceanogr. **44:** 1781-1787. doi:10.4319/lo.1999.44.7.1781

722 Hurrell, J. W., and C. Deser. 2009. North Atlantic climate variability: The role of the
723 North Atlantic Oscillation. J. Mar. Syst. **78:** 28-41.
724 doi:10.1016/j.jmarsys.2008.11.026

725 Ikeda, T. 1985. Metabolic rates of epipelagic marine zooplankton as a function of body
726 mass and temperature. Mar. Biol. **85:** 1-11. doi:10.1007/BF00396409

727 Ji, R., M. Edwards, D. L. Mackas, J. A. Runge, and A. C. Thomas. 2010. Marine
728 plankton phenology and life history in a changing climate: current research and
729 future directions. J. Plankton Res. **32:** 1355-1368. doi:10.1093/plankt/fbq062

730 Karl, D. M. 2010. Oceanic ecosystem time-series programs: Ten lessons learned.
731 Oceanography **23:** 104-125. doi:10.5670/oceanog.2010.27

732 Klausmeier, C. A., and E. Litchman. 2001. Algal games: The vertical distribution of
733 phytoplankton in poorly mixed water columns. Limnol. Oceanogr. **46:** 1998-
734 2007. doi:10.4319/lo.2001.46.8.1998

735 Koeller, P. and others. 2009. Basin-scale coherence in phenology of shrimps and
736 phytoplankton in the North Atlantic Ocean. Science **324:** 791-793.
737 doi:10.1126/science.1170987

738 Körtzinger, A., W. Koeve, P. Kähler, and L. Mintrop. 2001. C : N ratios in the mixed
739 layer during the productive season in the northeast Atlantic Ocean. Deep Sea
740 Res. Part I **48:** 661-688. doi:https://doi.org/10.1016/S0967-0637(00)00051-0

741 Kristiansen, T., K. F. Drinkwater, R. G. Lough, and S. Sundby. 2011. Recruitment
742 variability in North Atlantic cod and match-mismatch dynamics. PLoS One **6:**
743 e17456. doi:10.1371/journal.pone.0017456

744 Lampitt, R. S. 1985. Evidence for the seasonal deposition of detritus to the deep-sea
745 floor and its subsequent resuspension. Deep-Sea Res. Part A Oceanogr. Res.
746 Pap. **32:** 885-897. doi:10.1016/0198-0149(85)90034-2

747 Levitus, S. and others. 2012. World ocean heat content and thermosteric sea level
748 change (0–2000 m), 1955–2010. Geophys. Res. Lett. **39:** L10603.
749 doi:10.1029/2012GL051106

750 Lindemann, C., and M. A. St. John. 2014. A seasonal diary of phytoplankton in the
751 North Atlantic. Front. Mar. Sci. **1:** 1-6. doi:10.3389/fmars.2014.00037

752 Longhurst, A. R., and W. G. Harrison. 1989. The biological pump: profiles of plankton
753 production and consumption in the upper ocean. Prog. Oceanogr. **22:** 47-123.
754 doi:10.1016/0079-6611(89)90010-4

755 Llope, M., R. Anadón, J. Á. Sostres, and L. Viesca. 2007. Nutrients dynamics in the
756 southern Bay of Biscay (1993–2003): winter supply, stoichiometry, long-term
757 trends, and their effects on the phytoplankton community. J. Geophys. Res.:
758 Oceans **112:** C07029. doi:10.1029/2006JC003573

759 Llope, M., R. Anadón, L. Viesca, M. Quevedo, R. González-Quirós, and N. C. Stenseth.
760 2006. Hydrography of the southern Bay of Biscay shelf-break region: integrating
761 the multiscale physical variability over the period 1993-2003. J. Geophys. Res.:
762 Oceans **111:** C09021. doi:10.1029/2005JC002963

763 Mann, K. H., and J. R. N. Lazier. 2006. Dynamics of marine ecosystems. Biological–
764 Physical Interactions in the Oceans, 3rd ed. Blackwell.

765 Martinez, E., D. Antoine, F. D'Ortenzio, and C. de Boyer Montégut. 2011.
766 Phytoplankton spring and fall blooms in the North Atlantic in the 1980s and
767 2000s. J. Geophys. Res.: Oceans **116:** C11029. doi:10.1029/2010JC006836

768 McClain, C. R. 2009. A decade of satellite ocean color observations. Annu. Rev. Mar.
769 Sci. **1:** 19-42. doi:10.1146/annurev.marine.010908.163650

770 Monterey, G. I., and S. Levitus. 1997. Seasonal variability of mixed layer depth for the
771 World Ocean. NOAA Atlas NESDIS 14, US Government Printing Office.

Moore, C. M. and others. 2013. Processes and patterns of oceanic nutrient limitation. Nat. Geosci. **6:** 701-710. doi:10.1038/ngeo1765

NASA Goddard Space Flight Center, Ocean Ecology Laboratory, Ocean Biology Processing Group (OBPG). 2015a. Moderate-resolution Imaging Spectroradiometer (MODIS) Aqua Chlorophyll Data; 2013.1.1 Reprocessing. NASA OB.DAAC, Greenbelt, MD, USA. doi:10.5067/AQUA/MODIS/L3M/CHL/2014. Accessed on 2015/01/09.

NASA Goddard Space Flight Center, Ocean Ecology Laboratory, Ocean Biology Processing Group (OBPG). 2015b. Sea-viewing Wide Field-of-view Sensor (SeaWiFS) Chlorophyll Data; 2010.0 Reprocessing. NASA OB.DAAC, Greenbelt, MD, USA. doi:10.5067/AQUA/MODIS/L3M/CHL/2014. Accessed on 2015/01/09.

Nychka, D., S. Bandyopadhyay, D. Hammerling, F. Lindgren, and S. Sain. 2015. A Multiresolution Gaussian Process Model for the Analysis of Large Spatial Datasets. J. Comput. Graph. Stat. **24:** 579-599. doi:10.1080/10618600.2014.914946

Nychka, D., D. Hammerling, S. Sain, and N. Lenssen. 2016. LatticeKrig: Multiresolution Kriging Based on Markov Random Fields. R package version 6.2: www.image.ucar.edu/LatticeKrig. doi: 10.5065/D6HD7T1R.

O'Reilly, J. E. and others. 2000. Ocean color chlorophyll a algorithms for SeaWiFS, OC2, and OC4: Version 4, p. 9-23. *In* S. B. Hooker and E. R. Firestone [eds.], SeaWiFS Postlaunched Calibration and Validation Analyses, Part 3. NASA Tech. Memo 2000-206892,Vol. 11. NASA, GoddardSpace Flight Center.

Parsons, T. R., and C. M. Lalli. 1988. Comparative oceanic ecology of the plankton communities of the subarctic Atlantic and Pacific oceans. Oceanogr. Mar. Biol. Annu. Rev. **26:** 317-359.

Platt, T., C. Fuentes-Yaco, and K. T. Frank. 2003. Spring algal bloom and larval fish survival. Nature **423:** 398-399. doi:10.1038/423398b

R Core Team. 2017. R: A language and environment for statistical computing. R Foundation for Statistical Computing, Vienna, Austria. Available from http://www.R-project.org/.

Racault, M.-F., C. Le Quéré, E. Buitenhuis, S. Sathyendranath, and T. Platt. 2012. Phytoplankton phenology in the global ocean. Ecol. Indicators **14:** 152-163. doi:10.1016/j.ecolind.2011.07.010

809 Rantajärvi, E., R. Olsonen, S. Hällfors, J.-M. Leppänen, and M. Raateoja. 1998. Effect
810 of sampling frequency on detection of natural variability in phytoplankton:
811 unattended high-frequency measurements on board ferries in the Baltic Sea.
812 ICES J. Mar. Sci. **55:** 697-704. doi:10.1006/jmsc.1998.0384

813 Redfield, A. C. 1958. The biological control of chemical factors in the environment.
814 Am. Sci. **46:** 230A-221.

815 Reynolds, C. S. 2006. The ecology of phytoplankton. Cambridge University Press.

816 Reynolds, R. W., T. M. Smith, C. Liu, D. B. Chelton, K. S. Casey, and M. G. Schlax.
817 2007. Daily high-resolution-blended analyses for sea surface temperature. J.
818 Clim. **20:** 5473-5496. doi:10.1175/2007JCLI1824.1

819 RStudio Team. 2016. RStudio: Integrated Development Environment for R. RStudio,
820 Inc., Boston, MA. Avialable from http://www.rstudio.com.

821

822 Rumín-Caparrós, A., A. Sanchez-Vidal, C. González-Pola, G. Lastras, A. Calafat, and
823 M. Canals. 2016. Particle fluxes and their drivers in the Avilés submarine
824 canyon and adjacent slope, central Cantabrian margin, Bay of Biscay. Prog.
825 Oceanogr. **144:** 39-61. doi:https://doi.org/10.1016/j.pocean.2016.03.004

826 Sambrotto, R. N., H. J. Niebauer, J. J. Goering, and R. L. Iverson. 1986. Relationships
827 among vertical mixing, nitrate uptake, and phytoplankton growth during the
828 spring bloom in the southeast Bering Sea middle shelf. Cont. Shelf Res. **5:** 161-
829 198. doi:10.1016/0278-4343(86)90014-2

830 Sanders, R. and others. 2014. The biological carbon pump in the North Atlantic. Prog.
831 Oceanogr. **129:** 200-218. doi:10.1016/j.pocean.2014.05.005

832 Sarmiento, J. L., and N. Gruber. 2006. Ocean biogeochemical dynamics. Princeton
833 University Press.

834 Siegel, D. A., S. C. Doney, and J. A. Yoder. 2002. The North Atlantic spring
835 phytoplankton bloom and Sverdrup's critical depth hypothesis. Science **296:**
836 730-733. doi:10.1126/science.1069174

837 Sieracki, M. E., P. G. Verity, and D. K. Stoecker. 1993. Plankton community response
838 to sequential silicate and nitrate depletion during the 1989 North Atlantic spring
839 bloom. Deep Sea Res. Part II **40:** 213-225. doi:10.1016/0967-0645(93)90014-E

840 Smayda, T. J. 1970. The suspension and sinking of phytoplankton in the sea. Oceanogr.
841 Mar. Biol. Annu. Rev. **8:** 353-414. doi:10.1002/iroh.19720570110

842 Smetacek, V. S. 1985. Role of sinking in diatom life-history cycles: ecological,
843 evolutionary and geological significance. Mar. Biol. **84:** 239-251.
844 doi:10.1007/BF00392493

Somavilla Cabrillo, R., C. González-Pola, M. Ruiz-Villarreal, and A. Lavín Montero. 2011. Mixed layer depth (MLD) variability in the southern Bay of Biscay. Deepening of winter MLDs concurrent with generalized upper water warming trends? Ocean. Dynam. **61:** 1215-1235. doi:10.1007/s10236-011-0407-6

Somavilla, R., C. González-Pola, C. Rodriguez, S. A. Josey, R. F. Sánchez, and A. Lavín. 2009. Large changes in the hydrographic structure of the Bay of Biscay after the extreme mixing of winter 2005. J. Geophys. Res.: Oceans **114:** C01001. doi:10.1029/2008JC004974

Sverdrup, H. U. 1953. On conditions for the Vernal Blooming of Phytoplankton. J. Cons. Int. Explor. Mer. **18:** 287-295. doi:10.1093/icesjms/18.3.287

Taboada, F. G., and R. Anadón. 2012. Patterns of change in sea surface temperature in the North Atlantic during the last three decades: beyond mean trends. Clim. Change **115:** 419-431. doi:10.1007/s10584-012-0485-6

Taylor, J. R., and R. Ferrari. 2011. Shutdown of turbulent convection as a new criterion for the onset of spring phytoplankton blooms. Limnol. Oceanogr. **56:** 2293-2307. doi:10.4319/lo.2011.56.6.2293

Townsend, D. W., L. M. Cammen, P. M. Holligan, D. E. Campbell, and N. R. Pettigrew. 1994. Causes and consequences of variability in the timing of spring phytoplankton blooms. Deep Sea Res. Part I **41:** 747-765. doi:10.1016/0967-0637(94)90075-2

Ueyama, R., and B. C. Monger. 2005. Wind-induced modulation of seasonal phytoplankton blooms in the North Atlantic derived from satellite observations. Limnol. Oceanogr. **50:** 1820-1829. doi:10.4319/lo.2005.50.6.1820

Valdés, L., A. Lavín, M. L. Fernández de Puelles, M. Varela, R. Anadón, A. Miranda, J. Camiñas, and J. Mas. 2002. Spanish Ocean Observation System. IEO Core Project: studies on time series of oceanographic data. Elsevier Oceanogr. Ser. **66:** 99-105. doi:10.1016/S0422-9894(02)80014-9

Valdés, L. and others. 2007. A decade of sampling in the Bay of Biscay: What are the zooplankton time series telling us? Prog. Oceanogr. **74:** 98-114. doi:10.1016/j.pocean.2007.04.016

Varela, M. 1996. Phytoplankton ecology in the Bay of Biscay. Sci. Mar. **60:** 45-53.

Wickham, H. 2009. ggplot2: elegant graphics for data analysis. Springer.

Williams, R. G., and M. J. Follows. 2003. Physical transport of nutrients and the maintenance of biological production, p. 19-51. *In* M. J. R. Fasham [ed.], Ocean Biogeochemistry: The Role of the Ocean Carbon Cycle in Global Change. Springer.

Wood, S. N. 2006. Generalized additive models: an introduction with R. Chapman and Hall/CRC.

883 Wood, S. N., F. Scheipl, and J. J. Faraway. 2013. Straightforward intermediate rank
884 tensor product smoothing in mixed models. Stat. Comput. **23:** 341-360.
885 doi:10.1007/s11222-012-9314-z

886 Yentsch, C. S., and D. W. Menzel. 1963. A method for the determination of
887 phytoplankton chlorophyll and phaeophytin by fluorescence. Deep-Sea Res.
888 Oceanogr. Abstr. **10:** 221-231. doi:10.1016/0011-7471(63)90358-9

889 Yoder, J. A., C. R. McClain, G. C. Feldman, and W. E. Esaias. 1993. Annual cycles of
890 phytoplankton chlorophyll concentrations in the global ocean: A satellite view.
891 Glob. Biogeochem. Cycles **7:** 181-193. doi:10.1029/93GB02358

892 Yoshie, N., Y. Yamanaka, M. J. Kishi, and H. Saito. 2003. One dimensional ecosystem
893 model simulation of the effects of vertical dilution by the winter mixing on the
894 spring diatom bloom. J. Oceanogr. **59:** 563-571.
895 doi:10.1023/B:JOCE.0000009586.02554.d3

896

Acknowledgments

We thank all the people that helped in the establishment and maintenance of the time series collected at station E3 (Cudillero transect) used in this manuscript, especially those from the Areas of Ecology and Zoology of the University of Oviedo and the entire crew from the research vessel José Rioja. We also thank NASA Ocean Biology Processing Group (OBPG) and NOAA National Climatic Data Center (NCDC) for the production, availability and maintenance of the remote sensing data analyzed in this work. We are especially grateful to D. Tommasi, A. Rivera and S. Romero for their useful comments. Cudillero time series are part of the project RADIALES, Instituto Español de Oceanografía (IEO). This is a contribution of the Asturias Marine Observatory.

This research was co-funded by the agreement "Control a largo plazo de las condiciones químico-biológicas de la Plataforma Continental de Asturias" [Instituto Español de Oceanografía (IEO) and University of Oviedo] and by the project DOS MARES (CTM2010-21810- C03-02, Ministerio de Economía y Competitividad, Gobierno de España). R.G.-G. was supported by a FPU fellowship from the Ministerio de Educación, Cultura y Deporte, Gobierno de España.

Figure legends

Fig. 1. Map of the study area in the central Cantabrian Sea and its position in the Bay of Biscay. The shaded region around station E3 (dot) corresponds to the 0.25º x 0.25º quadrangle used to average satellite data.

Fig. 2. Intra- and interannual variations in: **(a)** nitrate and **(b)** Chl *a* concentrations over the first 200 m of the water column interpolated using kriging techniques, **(c)** depth-integrated nitrate (0-50 m, $\Sigma Nitrate_{0\text{-}50}$), **(d)** depth-integrated Chl *a* (0-200 m, $\Sigma Chl\ a_{0\text{-}200}$), **(e)** surface nitrate concentration ($[Nitrate]_{SFC}$) and **(f)** surface Chl *a* concentration ($[Chl\ a]_{SFC}$) from in situ (dots) and satellite (lines) observations. In all panels, years are separated by gray vertical dashed lines. In **(a)** and **(b)**, inner tick marks on the x-axis indicate those dates when data were collected, and data gaps spanning three or more consecutive months appear as vertical blank stripes. The thick contour line in **(a)** denotes the 1 μmol kg^{-1} nitrate isoline (i.e. the nitracline). Note the use of a log_{10} scale for Chl *a* in panels **(d)** and **(f)**.

Fig. 3. Seasonality of: **(a)** sea surface temperature (SST) based on satellite retrievals, **(b)** mixed layer depth (MLD) calculated using two different criteria (see *Material and methods*), **(c)** nitrate and **(d)** Chl *a* concentration over the first 200 m of the water column, **(e)** depth-integrated nitrate (0-50 m, $\Sigma Nitrate_{0\text{-}50}$), **(f)** depth-integrated Chl *a* (0-200 m, $\Sigma Chl\ a_{0\text{-}200}$), **(g)** surface nitrate concentration ($[Nitrate]_{SFC}$**)** and **(h)** surface satellite Chl *a* concentration ($[Chl\ a]_{SAT}$). Observed concentrations or integrated values (dots) and estimated seasonal cycles (solid lines in **a-b** and **e-h** or contour plots in **c-d**) are shown. In **(a-b)** and **(e-h)**, the 95% confidence intervals (shaded areas) associated to the estimated seasonal cycles are shown. Predicted values for each variable are based on the output of the generalized additive models (GAMs). The estimated degrees of freedom (edf) for each model are indicated. The inner tick marks on each axis in **(c)** and **(d)** indicate where data were available. The thick contour line in **(c)** denotes the 1 μmol kg^{-1} nitrate isoline (i.e. the nitracline). Note the use of a log_{10} scale for Chl *a*.

Fig. 4. Mean maximum Chl *a* concentration for each depth during the first half of the year and corresponding mean day of occurrence. Error bars indicate the 95 % confidence interval. Months are delimited by vertical dashed lines.

946 **Fig. 5.** Inter-annual variations of **(a)** maximum winter mixing depth (WMD_{max}) and
947 **(b)** depth-integrated nitrate (0-50 m, $\Sigma Nitrate_{0\text{-}50}$) at the WMD_{max} sampling date. Dot
948 color represents the winter month when WMD_{max} was measured (white, January; gray,
949 February; black, March). **(c)** Linear relationship between $\Sigma Nitrate_{0\text{-}50}$ at the WMD_{max}
950 sampling date and WMD_{max}. The shaded area represents the 95% confidence interval
951 associated to the linear correlation. The slope (*b*), proportion of variance explained (R^2)
952 and p-value of the relationship are shown.

953

954 **Fig. 6.** Predicted **(a)** additive effects on nitrate concentration and **(b)** multiplicative
955 effects on Chl *a* concentration of both maximum winter mixing depth (WMD_{max}) and
956 near-surface stratification ($MLD_{0.1}$) in March. These values were obtained based on the
957 best generalized additive model (GAM) of a set of proposed models to explore the
958 effect of WMD_{max} and $MLD_{0.1}$ on nitrate and Chl *a* concentrations (see Table 1). All
959 terms in the model had a p-value < 0.010 or < 0.050 for nitrate and Chl *a* concentration,
960 respectively. The estimated degrees of freedom (edf) are also shown. The inner tick
961 marks on each axis indicate where data were available.

962 **Fig. 7.** Observed (dot size) and predicted **(a)** nitrate and **(b)** Chl *a* concentrations at
963 surface (~ 0 m depth) in March (contour plot). Predicted values were obtained based on
964 the generalized additive model (GAM) in Table 2 that included an interaction term
965 between the maximum winter mixing depth (WMD_{max}) and the near-surface
966 stratification depth ($MLD_{0.1}$) in March. This interaction term had a p-value < 0.010 or <
967 0.050 for nitrate and Chl *a* concentration, respectively. The estimated degrees of
968 freedom (edf) for each model are indicated. The dark gray triangles on the top left
969 corners delimit those combinations of WMD_{max} and $MLD_{0.1}$ that are not possible
970 (WMD_{max} cannot be shallower than $MLD_{0.1}$). Note that predicted Chl *a* concentrations
971 are shown in $\log_{10}$ scale.

972

973 **Fig. 8.** Linear relationship between the new primary production (PP_{new}) in the upper
974 50 m of the water column between February and April and the maximum winter mixing
975 depth (WMD_{max}). The shaded area represents the 95% confidence interval associated to
976 the linear correlation. The slope (*b*), proportion of variance explained (R^2) and p-value
977 of the relationship are shown.

978 **Fig. 9** Sea surface temperatures (SST, light gray line) and Chl *a* concentrations ([Chl
979 *a*]$_{SAT,}$ dots) from 1997 to 2012 based on satellite retrievals. Dot color indicates the
980 sensor used to get the [Chl a]$_{SAT}$ measurements (white for SeaWifs and black for Aqua
981 MODIS). Estimated seasonal cycles for SST (dark gray line) and [Chl *a*]$_{SAT}$ (black line)
982 and their associated 95% confidence intervals (shaded areas) are based on the
983 generalized additive model (GAM) predictions. The estimated degrees of freedom (edf)
984 of the model varied between 16.19 and 18.53 for SST or between 3.19 and 13.42 for
985 [Chl *a*]$_{SAT}$. Vertical solid lines indicate the maximum estimated [Chl *a*]$_{SAT}$ during the
986 spring bloom. The initiation and termination day of the spring bloom are marked with
987 vertical dashed lines. Note that [Chl *a*]$_{SAT}$ is shown in $\log_{10}$ scale and that the beginning
988 of the seasonal cycle is set to July 15th (or 14th in a leap year).

989

990 **Fig. 10.** Impact of the intensity and timing of the maximum winter mixing depth
991 (WMD_{max} and WMD_{max} sampling date, respectively) on spring bloom metrics: **(a-b)**
992 bloom rise, **(c-d)** bloom decay, **(e-f)** max Chl *a*, **(g-h)** max Chl *a* timing and **(i-j)** bloom
993 span. The spring bloom metrics were derived from a generalized additive model (GAM)
994 based on satellite data. The shaded areas associated to each linear relationship depict the
995 95% confidence intervals. The slope (*b*) and proportion of variance explained (R^2) of
996 each relationship are shown. Those linear regressions with a p-value <0.050 are
997 indicated with a *. Note that max Chl *a* is shown in $\log_{10}$ scale.

998 **Fig. 11. (a)** Variations in the slope of the linear relationships between maximum
999 winter mixing depth (WMD_{max}) and the Sea Surface Temperature (SST) based on
1000 satellite retrievals at different day lags (1993-2012). **(b)** Long-term linear trends in SST
1001 (1981-2012) for each day of the year. Dashed horizontal lines indicate zero values.
1002 Shaded areas depict the 95% confidence intervals associated with the regression slopes.

Tables

Table 1. Results from the model selection for the assessment of the effect of winter mixing depth (WMD_{max}) and our proxy for the thickness of the surface stratified layer ($MLD_{0.1}$) on nitrate and Chl *a* concentration at all depths (both represented as *y* in the formulas) in March. All models included an intercept (a) and an error term (ε). In addition, the generalized additive models (GAMs) incorporated through a smooth function (f, see *Supporting information* for further details) the influence of depth (z), or also the effect of the interaction (te) between $MLD_{0.1}$ or WMD_{max} and depth. We report for each model the Akaike Information Criterion (AIC) and its associated weight (Burnham and Anderson 2002), and the proportion of variance explained (R^2). In all cases, the overall model had a p-value < 0.001.

		Nitrate			Chl *a*		
Model	**What does the model estimates?**	**AIC**	**AIC weight**	**R^2**	**AIC**	**AIC weight**	**R^2**
$y = a + \varepsilon$	Null model (includes only an intercept).	598.80	0.00	0.00	222.61	0.00	0.00
$y = a + f(z) + \varepsilon$	Effect of depth.	534.20	0.00	0.36	139.50	0.00	0.47
$y = a + f(z) + te(WMD_{max}, z) + \varepsilon$	Effect of winter mixing through the water column while accounting for the influence of depth.	452.09	0.00	0.64	122.99	0.00	0.56
$y = a + f(z) + te(MLD_{0.1}, z) + \varepsilon$	Effect of stratification through the water column while accounting for the influence of depth.	513.04	0.00	0.48	131.77	0.00	0.54
$y = a + f(z) + te(MLD_{0.1}, z) + te(WMD_{max}, z) + \varepsilon$	Combined effect of stratification and winter mixing through the water column while accounting for the influence of depth.	419.50	1.00	0.73	101.29	1.00	0.65

Table 2. Results from the model selection for the assessment of the effect of winter mixing depth (WMD_{max}) and our proxy for the thickness of the surface stratified layer ($MLD_{0.1}$) on nitrate and Chl *a* concentration (both represented as *y* in the formulas) at the surface (~ 0 m depth) in March. All models included an intercept (a) and an error term (ε). In addition, the generalized additive models (GAMs) incorporated a smooth function (f see *Supporting information* for further details) to estimate the effect of WMD_{max}, $MLD_{0.1}$ or their interaction (te, last model). We report for each model the Akaike Information Criterion (AIC) and its associated weight (Burnham and Anderson 2002), and the proportion of variance explained (R^2). The p-values for the overall model are also shown.

		Nitrate				Chl *a*			
Model	**What does the model estimates?**	**AIC**	**AIC weight**	**R^2**	**p-value**	**AIC**	**AIC weight**	**R^2**	**p-value**
$y = a + \varepsilon$	Null model (includes only an intercept).	60.63	0.00	0.00	0.000	20.12	0.00	0.00	0.572
$y = a + f(WMD_{max}) + \varepsilon$	Effect of winter mixing.	59.92	0.00	0.17	0.132	17.42	0.02	0.29	0.049
$y = a + (MLD_{0.1}) + \varepsilon$	Effect of stratification.	51.51	0.21	0.52	0.002	19.78	0.01	0.15	0.165
$y = a + f(MLD_{0.1}) + f(WMD_{max}) + \varepsilon$	Independent combined effect of stratification and winter mixing.	49.70	0.53	0.63	0.003	15.14	0.06	0.48	0.030
$y = a + te(WMD_{max}, MLD_{0.1}) + \varepsilon$	Interactive combined effect of winter mixing and stratification.	51.16	0.26	0.64	0.008	9.72	0.91	0.75	0.016

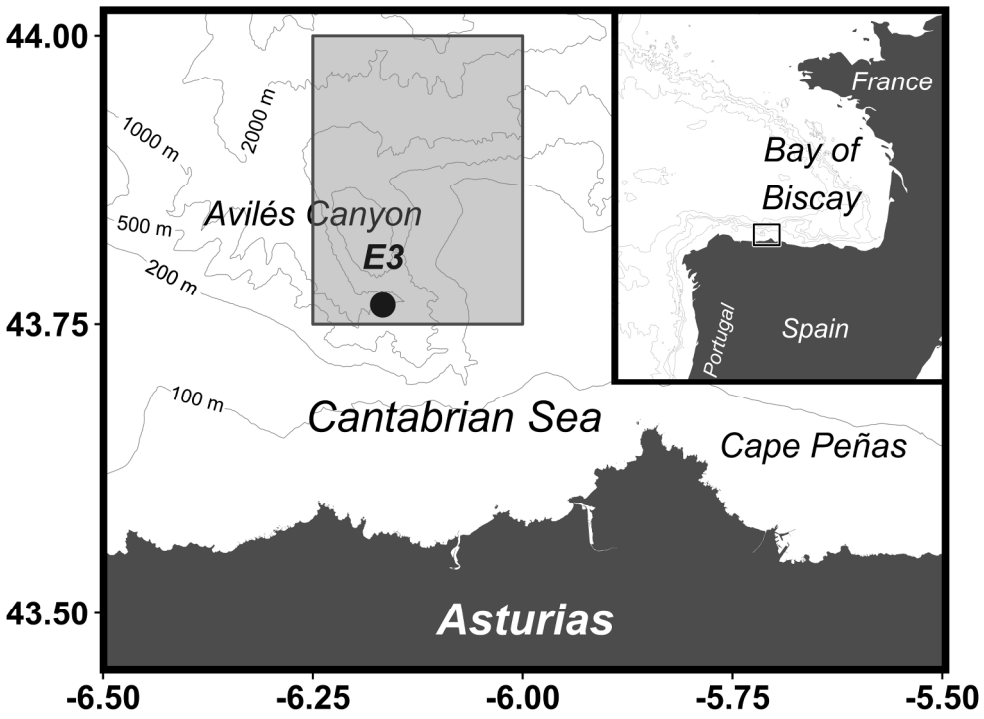

Fig. 1. Map of the study area in the central Cantabrian Sea and its position in the Bay of Biscay. The shaded region around station E3 (dot) corresponds to the 0.25º x 0.25º quadrangle used to average satellite data.

642x475mm (96 x 96 DPI)

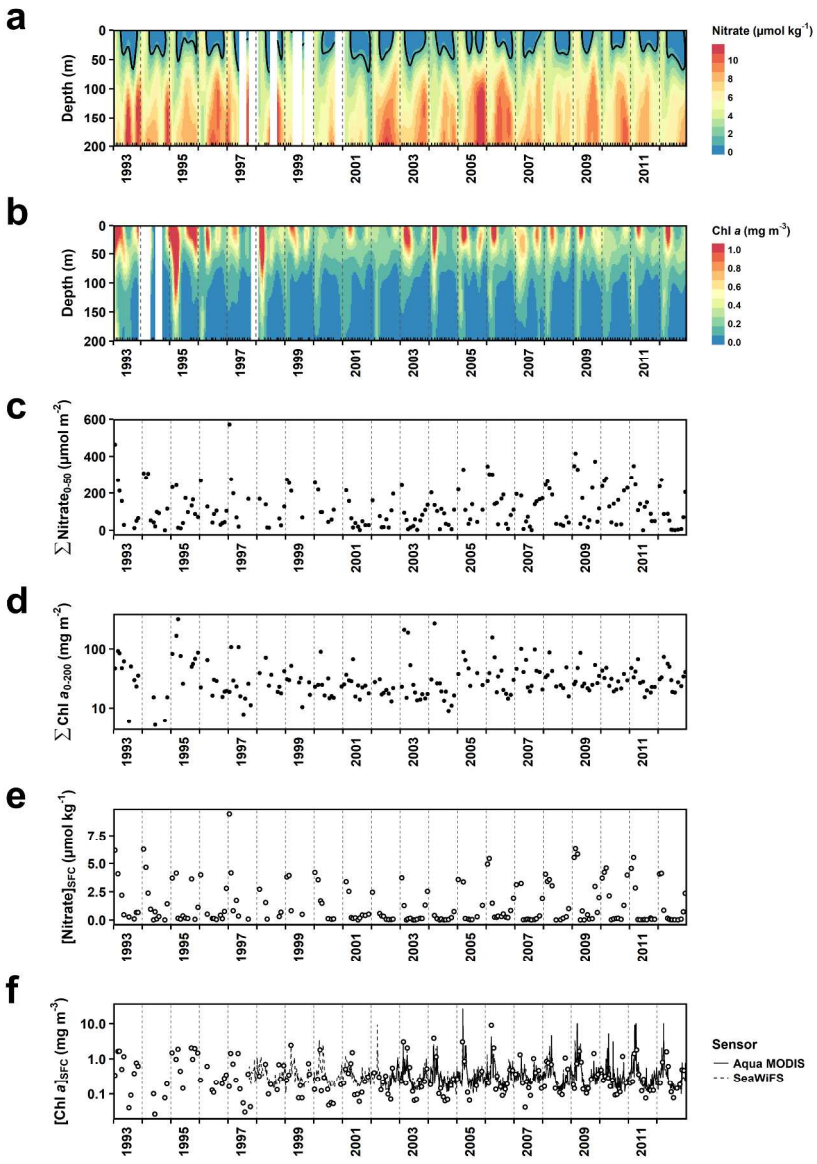

Fig. 2. Intra- and interannual variations in: (a) nitrate and (b) Chl a concentrations over the first 200 m of the water column interpolated using kriging techniques, (c) depth-integrated nitrate (0-50 m, ΣNitrate0-50), (d) depth-integrated Chl a (0-200 m, ΣChl a0-200), (e) surface nitrate concentration ([Nitrate]SFC) and (f) surface Chl a concentration ([Chl a]SFC) from in situ (dots) and satellite (lines) observations. In all panels, years are separated by gray vertical dashed lines. In (a) and (b), inner tick marks on the x-axis indicate those dates when data were collected, and data gaps spanning three or more consecutive months appear as vertical blank stripes. The thick contour line in (a) denotes the 1 µmol kg−1 nitrate isoline (i.e. the nitracline). Note the use of a log10 scale for Chl a in panels (d) and (f).

762x1048mm (96 x 96 DPI)

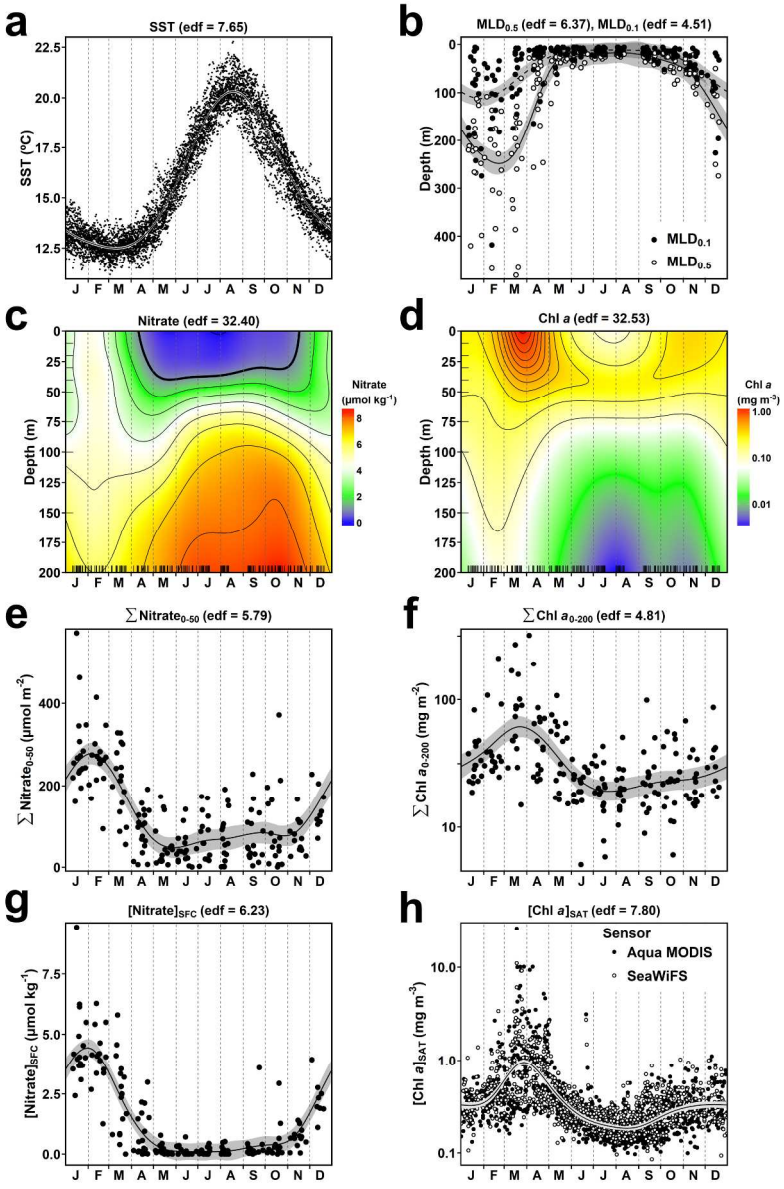

Fig. 3. Seasonality of: (a) sea surface temperature (SST) based on satellite retrievals, (b) mixed layer depth (MLD) calculated using two different criteria (see Material and methods), (c) nitrate and (d) Chl a concentration over the first 200 m of the water column, (e) depth-integrated nitrate (0-50 m, ΣNitrate0-50), (f) depth-integrated Chl a (0-200 m, ΣChl a0-200), (g) surface nitrate concentration ([Nitrate]SFC) and (h) surface satellite Chl a concentration ([Chl a]SAT). Observed concentrations or integrated values (dots) and estimated seasonal cycles (solid lines in a-b and e-h or contour plots in c-d) are shown. In (a-b) and (e-h), the 95% confidence intervals (shaded areas) associated to the estimated seasonal cycles are shown. Predicted values for each variable are based on the output of the generalized additive models (GAMs). The estimated degrees of freedom (edf) for each model are indicated. The inner tick marks on each axis in (c) and (d) indicate where data were available. The thick contour line in (c) denotes the 1 μmol kg−1 nitrate isoline (i.e. the nitracline). Note the use of a log10 scale for Chl a.

610x917mm (96 x 96 DPI)

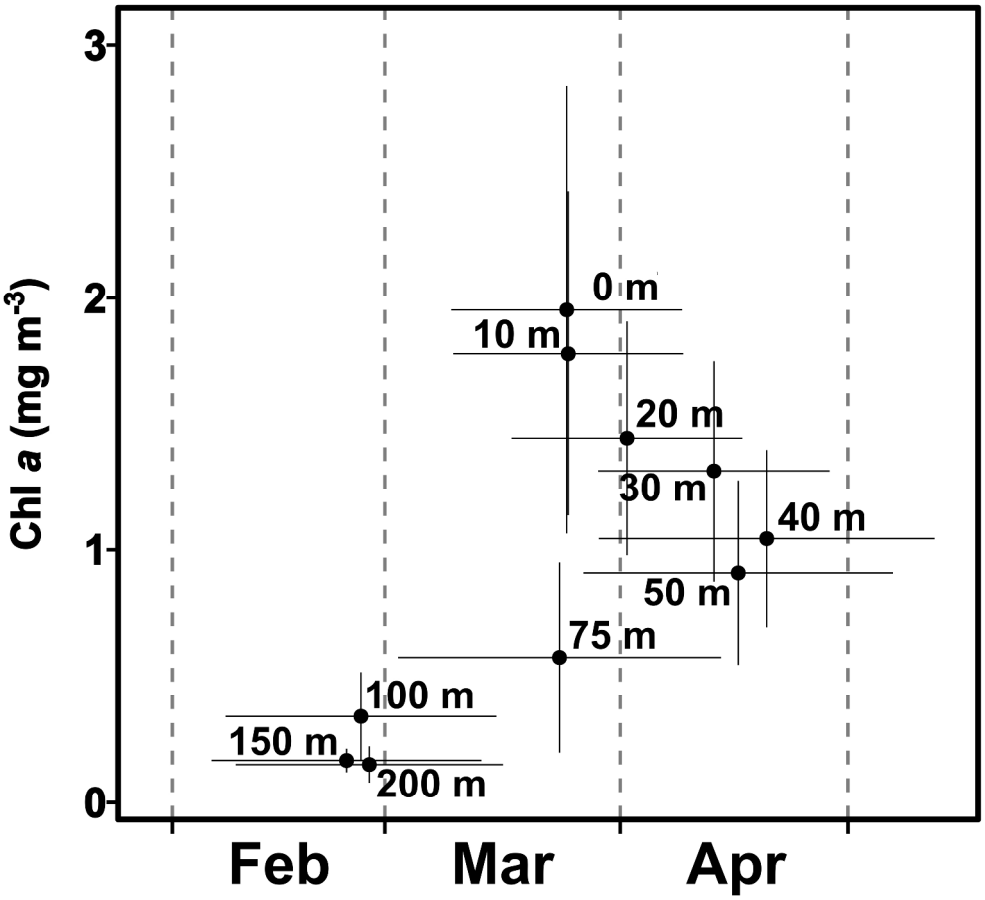

Fig. 4. Mean maximum Chl a concentration for each depth during the first half of the year and corresponding mean day of occurrence. Error bars indicate the 95 % confidence interval. Months are delimited by vertical dashed lines.

955x858mm (96 x 96 DPI)

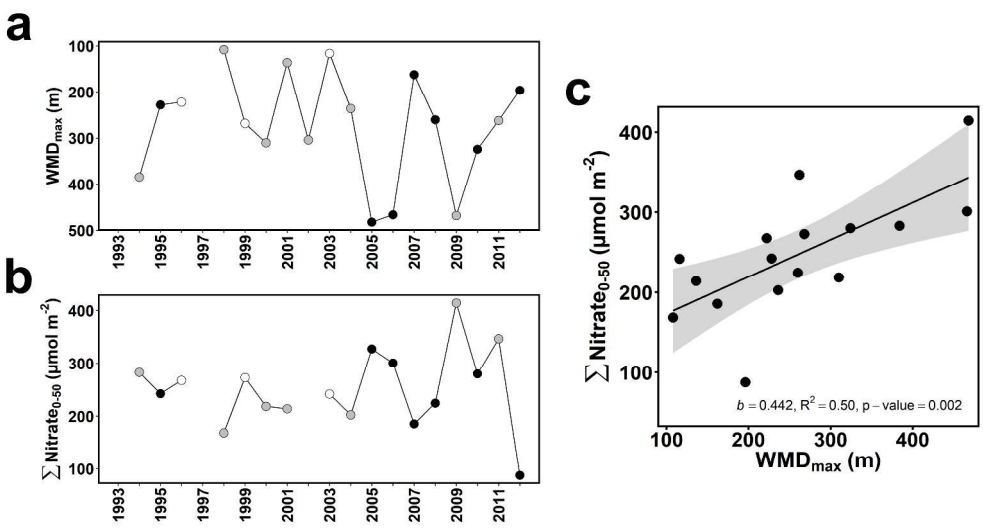

Fig. 5. Inter-annual variations of (a) maximum winter mixing depth (WMDmax) and (b) depth-integrated nitrate (0-50 m, ΣNitrate0-50) at the WMDmax sampling date. Dot color represents the winter month when WMDmax was measured (white, January; gray, February; black, March). (c) Linear relationship between ΣNitrate0-50 at the WMDmax sampling date and WMDmax. The shaded area represents the 95% confidence interval associated to the linear correlation. The slope (b), proportion of variance explained (R2) and p-value of the relationship are shown.

1236x674mm (96 x 96 DPI)

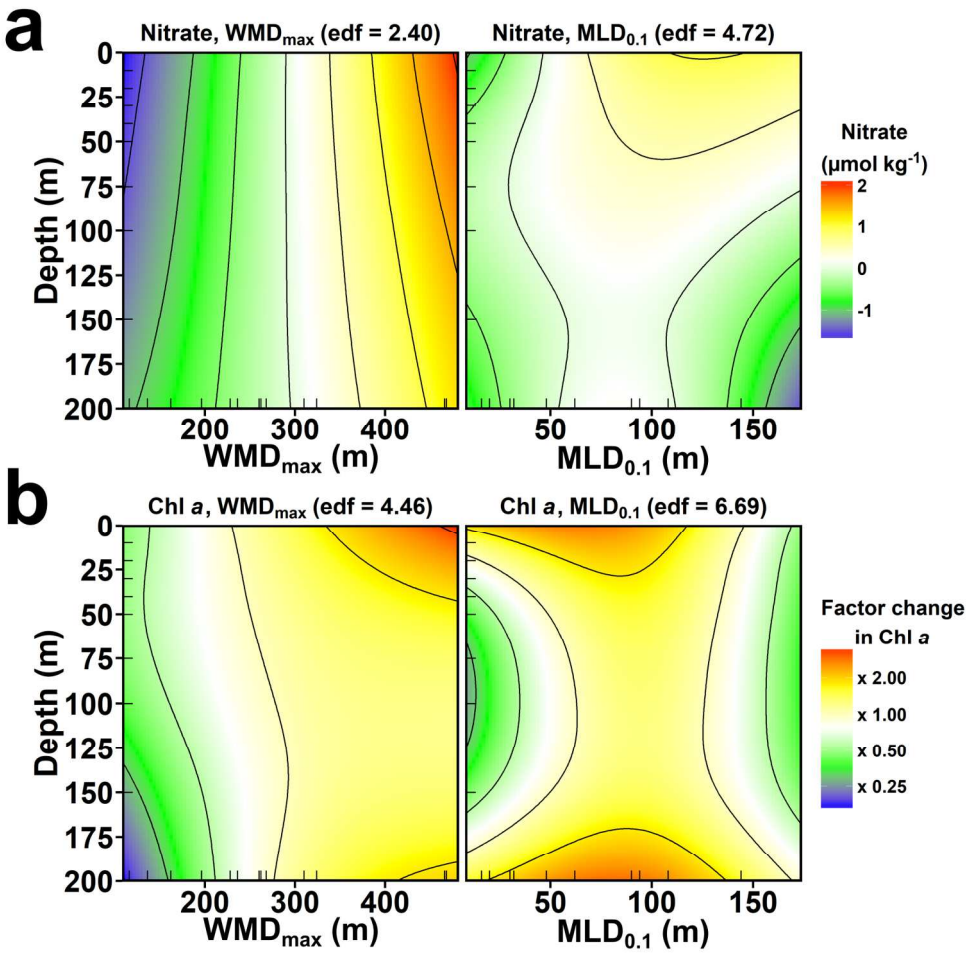

Fig. 6. Predicted (a) additive effects on nitrate concentration and (b) multiplicative effects on Chl a concentration of both maximum winter mixing depth (WMDmax) and near-surface stratification (MLD0.1) in March. These values were obtained based on the best generalized additive model (GAM) of a set of proposed models to explore the effect of WMDmax and MLD0.1 on nitrate and Chl a concentrations (see Table 1). All terms in the model had a p-value < 0.010 or < 0.050 for nitrate and Chl a concentration, respectively. The estimated degrees of freedom (edf) are also shown. The inner tick marks on each axis indicate where data were available.

497x480mm (96 x 96 DPI)

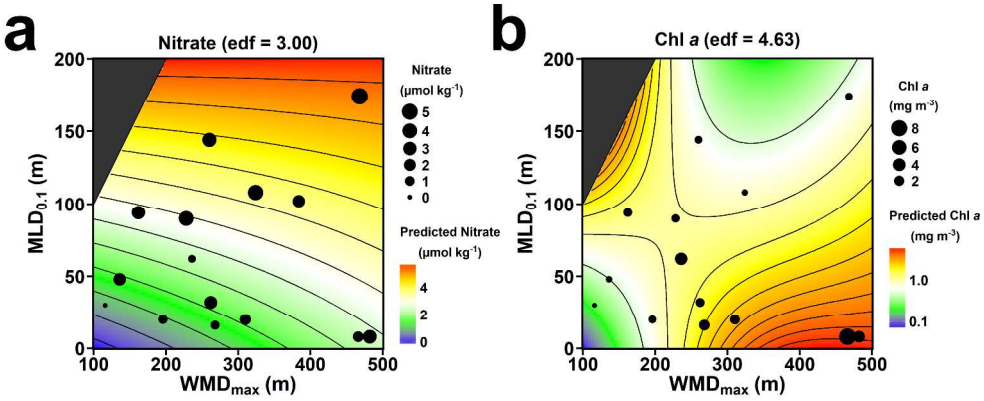

Fig. 7. Observed (dot size) and predicted (a) nitrate and (b) Chl a concentrations at surface (~ 0 m depth) in March (contour plot). Predicted values were obtained based on the generalized additive model (GAM) in Table 2 that included an interaction term between the maximum winter mixing depth (WMDmax) and the near-surface stratification depth (MLD0.1) in March. This interaction term had a p-value < 0.010 or < 0.050 for nitrate and Chl a concentration, respectively. The estimated degrees of freedom (edf) for each model are indicated. The dark gray triangles on the top left corners delimit those combinations of WMDmax and MLD0.1 that are not possible (WMDmax cannot be shallower than MLD0.1). Note that predicted Chl a concentrations are shown in log10 scale.

1394x597mm (96 x 96 DPI)

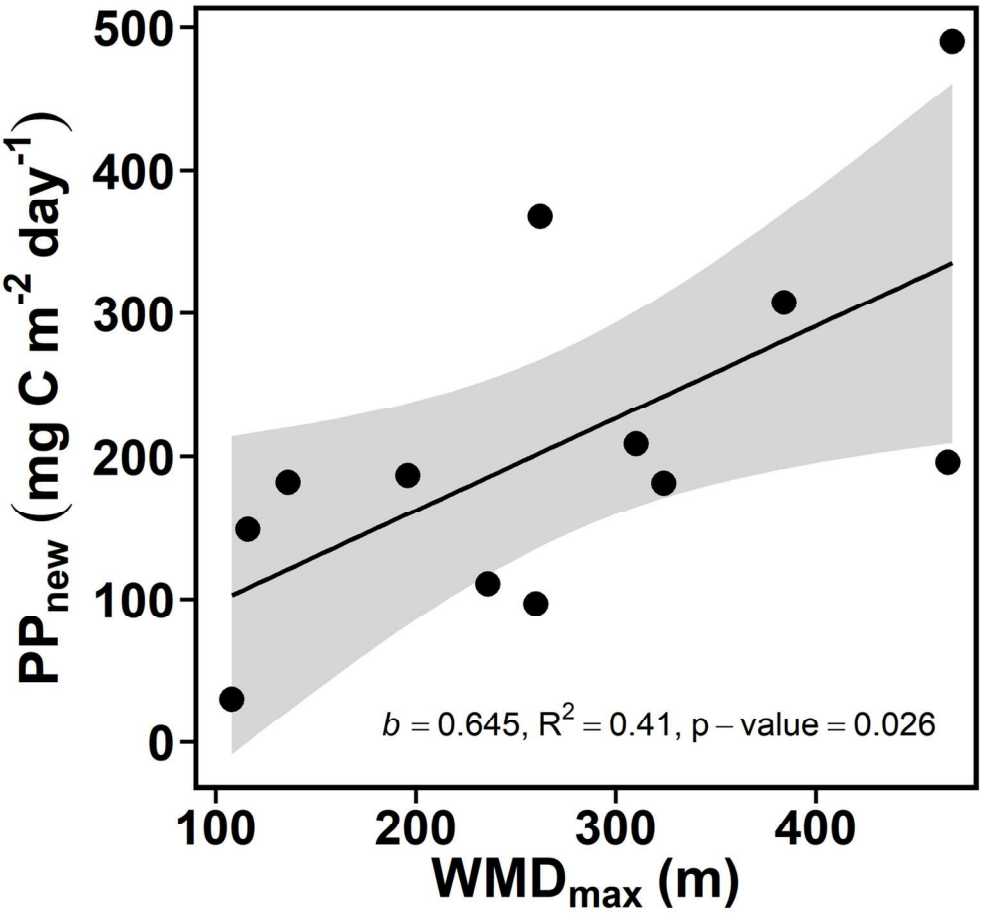

Fig. 8. Linear relationship between the new primary production (PPnew) in the upper 50 m of the water column between February and April and the maximum winter mixing depth (WMDmax). The shaded area represents the 95% confidence interval associated to the linear correlation. The slope (b), proportion of variance explained (R2) and p-value of the relationship are shown.

139x130mm (300 x 300 DPI)

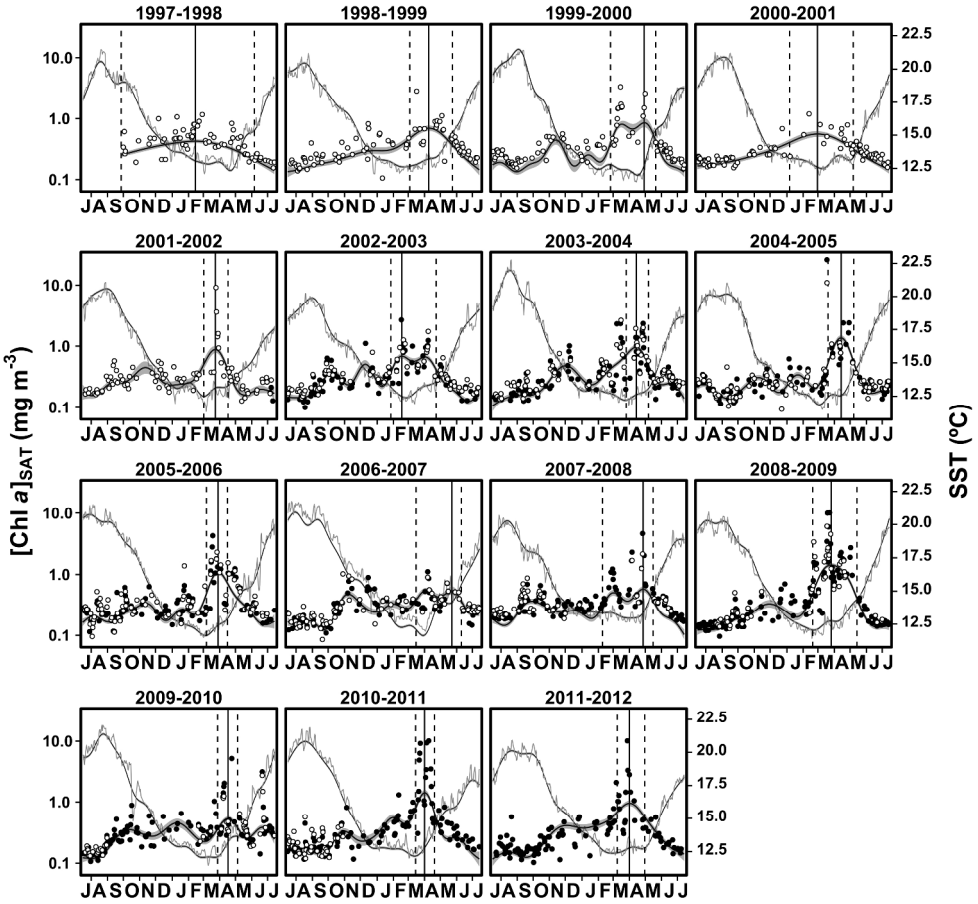

Fig. 9 Sea surface temperatures (SST, light gray line) and Chl a concentrations ([Chl a]SAT, dots) from 1997 to 2012 based on satellite retrievals. Dot color indicates the sensor used to get the [Chl a]SAT measurements (white for SeaWifs and black for Aqua MODIS). Estimated seasonal cycles for SST (dark gray line) and [Chl a]SAT (black line) and their associated 95% confidence intervals (shaded areas) are based on the generalized additive model (GAM) predictions. The estimated degrees of freedom (edf) of the model varied between 16.19 and 18.53 for SST or between 3.19 and 13.42 for [Chl a]SAT. Vertical solid lines indicate the maximum estimated [Chl a]SAT during the spring bloom. The initiation and termination day of the spring bloom are marked with vertical dashed lines. Note that [Chl a]SAT is shown in log10 scale and that the beginning of the seasonal cycle is set to July 15th (or 14th in a leap year).

987x909mm (96 x 96 DPI)

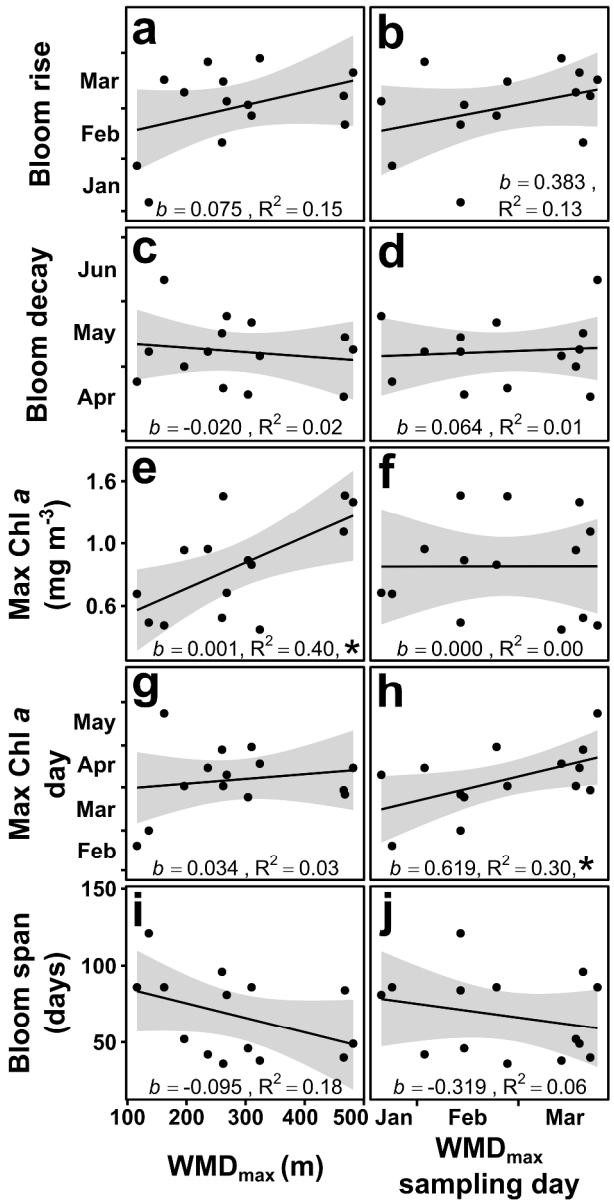

Fig. 10. Impact of the intensity and timing of the maximum winter mixing depth (WMDmax and WMDmax sampling date, respectively) on spring bloom metrics: (a-b) bloom rise, (c-d) bloom decay, (e-f) max Chl a, (g-h) max Chl a timing and (i-j) bloom span. The spring bloom metrics were derived from a generalized additive model (GAM) based on satellite data. The shaded areas associated to each linear relationship depict the 95% confidence intervals. The slope (b) and proportion of variance explained (R2) of each relationship are shown. Those linear regressions with a p-value <0.050 are indicated with a *. Note that max Chl a is shown in log10 scale.

734x1418mm (96 x 96 DPI)

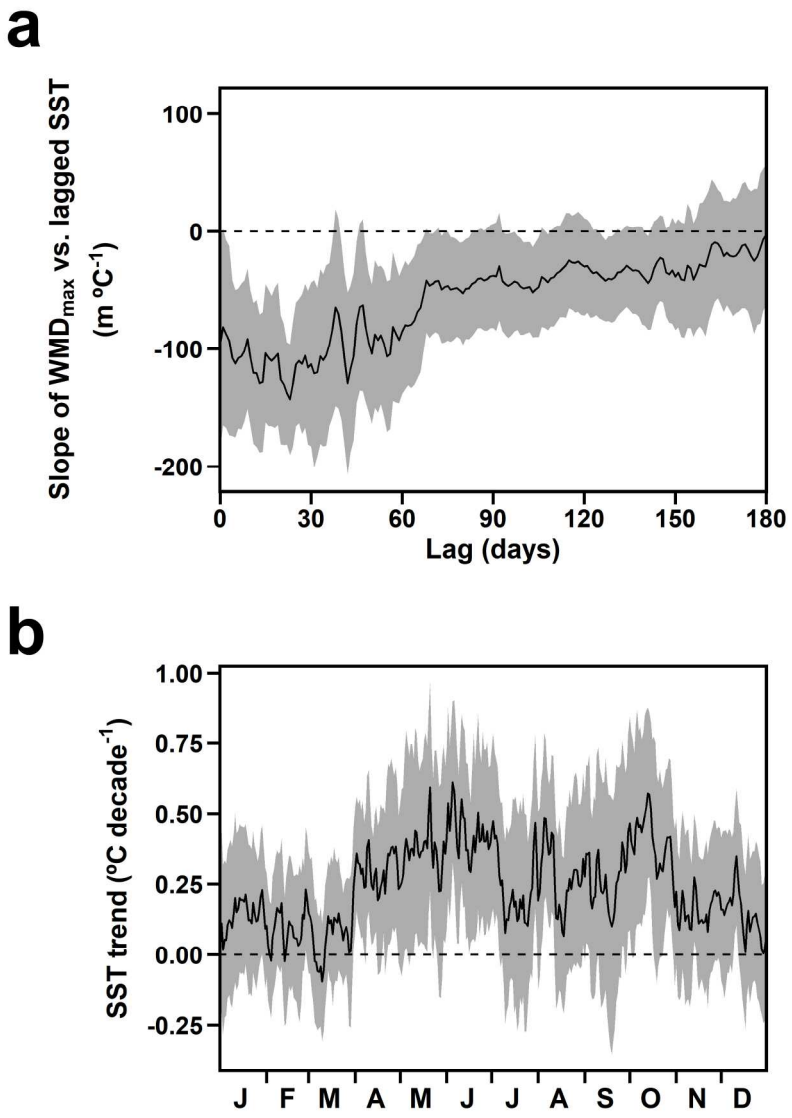

Fig. 11. (a) Variations in the slope of the linear relationships between maximum winter mixing depth (WMDmax) and the Sea Surface Temperature (SST) based on satellite retrievals at different day lags (1993-2012). (b) Long-term linear trends in SST (1981-2012) for each day of the year. Dashed horizontal lines indicate zero values. Shaded areas depict the 95% confidence intervals associated with the regression slopes.

535x789mm (96 x 96 DPI)

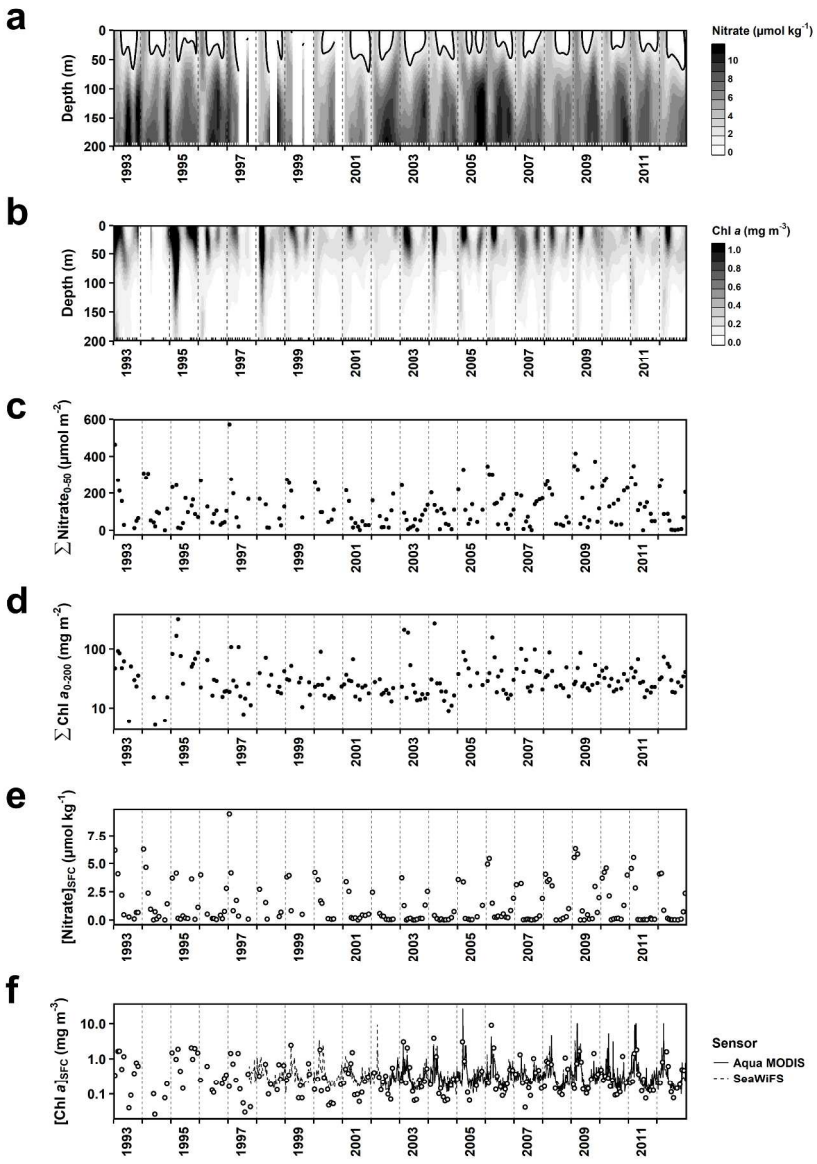

Fig. 2. Intra- and interannual variations in: (a) nitrate and (b) Chl a concentrations over the first 200 m of the water column interpolated using kriging techniques, (c) depth-integrated nitrate (0-50 m, ΣNitrate0-50), (d) depth-integrated Chl a (0-200 m, ΣChl a0-200), (e) surface nitrate concentration ([Nitrate]SFC) and (f) surface Chl a concentration ([Chl a]SFC) from in situ (dots) and satellite (lines) observations. In all panels, years are separated by gray vertical dashed lines. In (a) and (b), inner tick marks on the x-axis indicate those dates when data were collected, and data gaps spanning three or more consecutive months appear as vertical blank stripes. The thick contour line in (a) denotes the 1 µmol kg−1 nitrate isoline (i.e. the nitracline). Note the use of a log10 scale for Chl a in panels (d) and (f).

762x1048mm (96 x 96 DPI)

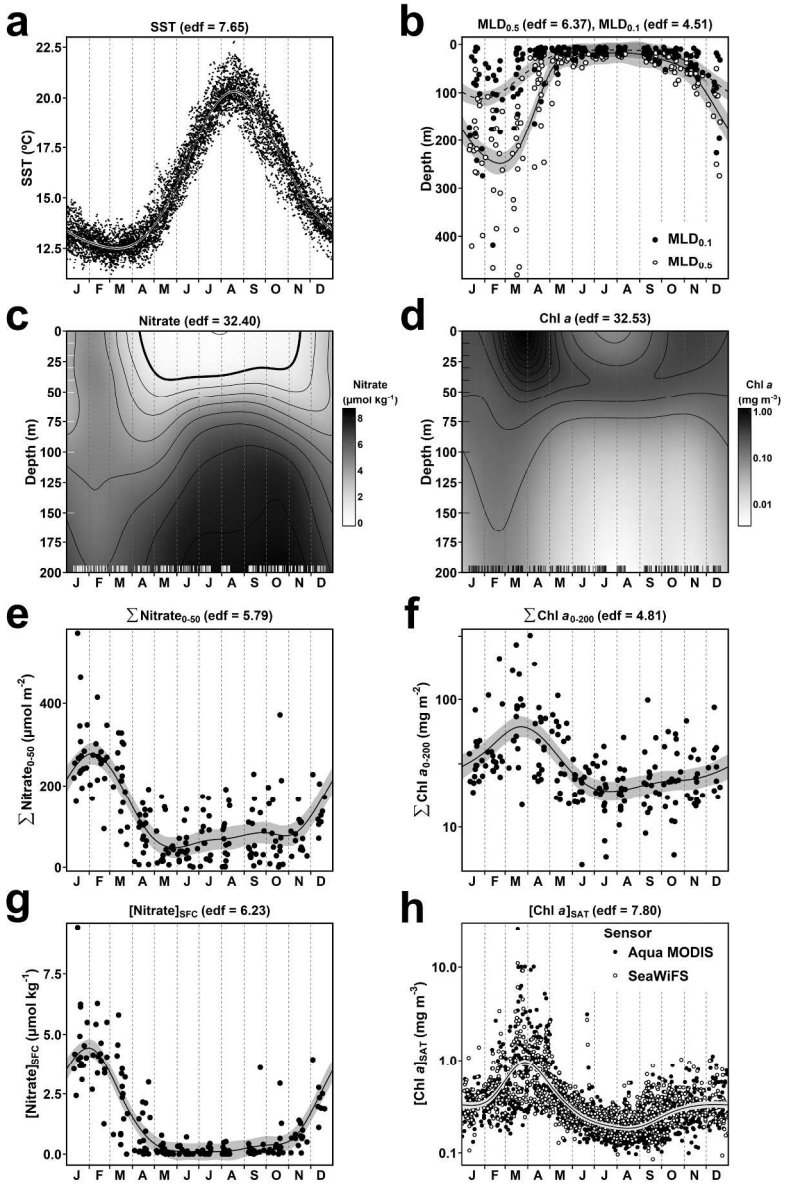

Fig. 3. Seasonality of: (a) sea surface temperature (SST) based on satellite retrievals, (b) mixed layer depth (MLD) calculated using two different criteria (see Material and methods), (c) nitrate and (d) Chl a concentration over the first 200 m of the water column, (e) depth-integrated nitrate (0-50 m, ΣNitrate0-50), (f) depth-integrated Chl a (0-200 m, ΣChl a0-200), (g) surface nitrate concentration ([Nitrate]SFC) and (h) surface satellite Chl a concentration ([Chl a]SAT). Observed concentrations or integrated values (dots) and estimated seasonal cycles (solid lines in a-b and e-h or contour plots in c-d) are shown. In (a-b) and (e-h), the 95% confidence intervals (shaded areas) associated to the estimated seasonal cycles are shown. Predicted values for each variable are based on the output of the generalized additive models (GAMs). The estimated degrees of freedom (edf) for each model are indicated. The inner tick marks on each axis in (c) and (d) indicate where data were available. The thick contour line in (c) denotes the 1 μmol kg−1 nitrate isoline (i.e. the nitracline). Note the use of a log10 scale for Chl a.

610x917mm (96 x 96 DPI)

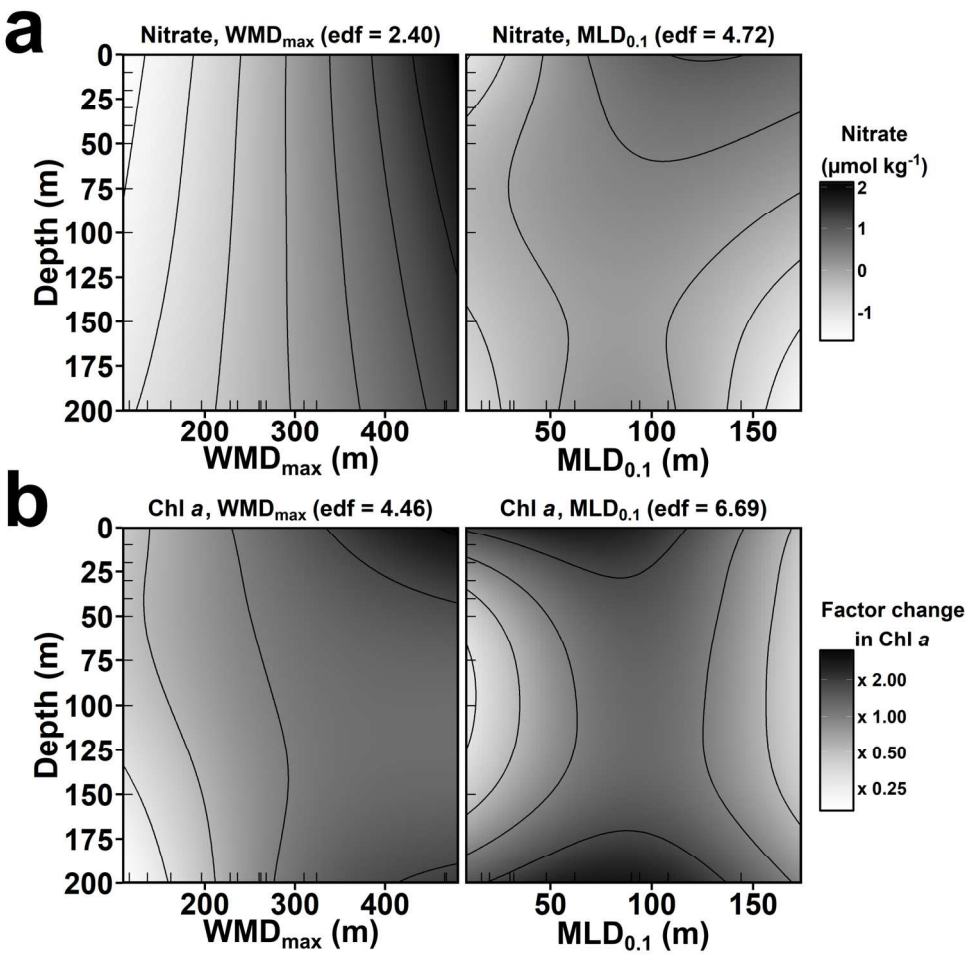

Fig. 6. Predicted (a) additive effects on nitrate concentration and (b) multiplicative effects on Chl a concentration of both maximum winter mixing depth (WMDmax) and near-surface stratification (MLD0.1) in March. These values were obtained based on the best generalized additive model (GAM) of a set of proposed models to explore the effect of WMDmax and MLD0.1 on nitrate and Chl a concentrations (see Table 1). All terms in the model had a p-value < 0.010 or < 0.050 for nitrate and Chl a concentration, respectively. The estimated degrees of freedom (edf) are also shown. The inner tick marks on each axis indicate where data were available.

497x480mm (96 x 96 DPI)

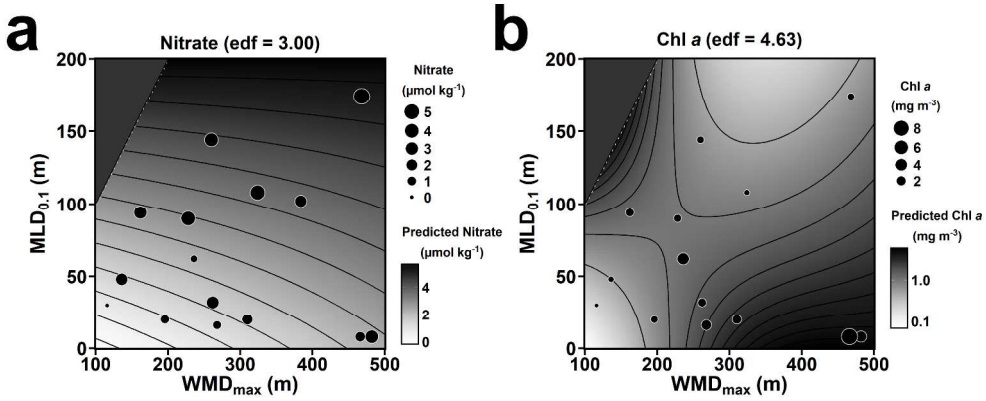

Fig. 7. Observed (dot size) and predicted (a) nitrate and (b) Chl a concentrations at surface (~ 0 m depth) in March (contour plot). Predicted values were obtained based on the generalized additive model (GAM) in Table 2 that included an interaction term between the maximum winter mixing depth (WMDmax) and the near-surface stratification depth (MLD0.1) in March. This interaction term had a p-value < 0.010 or < 0.050 for nitrate and Chl a concentration, respectively. The estimated degrees of freedom (edf) for each model are indicated. The dark gray triangles on the top left corners delimit those combinations of WMDmax and MLD0.1 that are not possible (WMDmax cannot be shallower than MLD0.1). Note that predicted Chl a concentrations are shown in log10 scale.

1394x597mm (96 x 96 DPI)

Supporting information

Supporting text

Details about Generalized Additive Models (GAMs)

Generalized Additive Models (GAMs, Hastie and Tibshirani 1990; Wood 2006) are statistical regression models characterized by the inclusion of smooth functions (*f*) to describe the relationship between response and predictor variables. In this way, GAMs are not tied to an a priori specification of the functional relationship between dependent and independent variables (e.g. linear or quadratic). Instead, these models estimate a linear combination of local cubic basis functions to ensure that each particular observation affects only the nearby fit. Among a variety of candidate smooth functions, tensor products (*te*) are particularly appropriate to describe n-dimensional non-linear effects of variables measured in different units (Wood 2006). These smooths are constructed by combining marginal smooths (or marginal basis) for each term involved in the interaction. All these characteristics make GAMs ideally suited to analyze complex non-linear relationships commonly found in the marine environment (see for example Stenseth et al. 2006; Murase et al. 2009; Kvile et al. 2016).

The degree of nonlinearity of a smooth predictor function *f* depends on the number of effective degrees of freedom, *edf*. Larger *edf* corresponds to smooth functions describing more complex nonlinear effects. It is thus necessary to find a balance between the complexity and the predictive ability of each smooth function in the model to avoid overfitting. To do that, an optimal *edf* value is determined during model fit by cross-validation. Here we followed recommendations by Wood (2006) and employed the generalized cross-validation score (GCV), after setting an upper limit for the *edf* (*k*) (i.e.

the greatest number of *edf* that the model can have). One degree of freedom is usually lost by this upper limit to the identifiability constraint on the smooth (Wood 2006).

The following table includes the specifications for the GAMs presented in the main text:

Analysis (model)	Smooth terms	Maximum *edf* (*k**)
Seasonality of physical variables, vertically integrated Chl *a* and $[\text{Chl } a]_{SAT}$ (Eq. 1 in the main text).	Cyclic cubic regression spline for the day of the year (*t*).	$k_t = 10^{**}$
Seasonality of nitrate and Chl *a* at different depths (Eq. 2 in the main text).	Tensor product among *t* and depth (*z*) with marginal basis: - *t:* cyclic cubic spline. - *z:* thin-plate regression spline.	$k_t = 9^{**}$ $k_z = 8$
Effect of winter mixing (WMD_{max}) and near-surface stratification ($MLD_{0.1}$) on Chl *a* and nitrate through the water column during the spring bloom (Table 1 in the main text).	Thin-plate regression splines for the effect of *z*, WMD_{max} or $MLD_{0.1}$, and to construct the marginal bases in the tensor products.	$k_z = 8$ $k_{WMDmax} = 3$ $k_{MLD0.1} = 3$
Effect of WMD_{max} and $MLD_{0.1}$ on surface Chl *a* and nitrate or vertically integrated Chl *a* during the spring bloom (Table 2 in the main text).	Thin-plate regression splines for the effect of WMD_{max} or $MLD_{0.1}$, and to construct the marginal bases in the tensor products.	$k_{WMDmax} = 3$ $k_{MLD0.1} = 3$
Interannual changes in seasonality of $[\text{Chl } a]_{SAT}$ or SST (Eq. 4 in the main text).	Thin plate regression spline for *t*|*year*.	$k_{[Chl\ a]SAT} = 15$ $k_{SST} = 20$

* *k* was set in each case to a value that provided a reliable model output; i.e. a value large enough to capture the main variability patterns in the data without overfitting.

** Note that for cyclic cubic regression splines, one degree of freedom is lost due to the constrain of this particular type of spline function.

33 **Supporting figure**

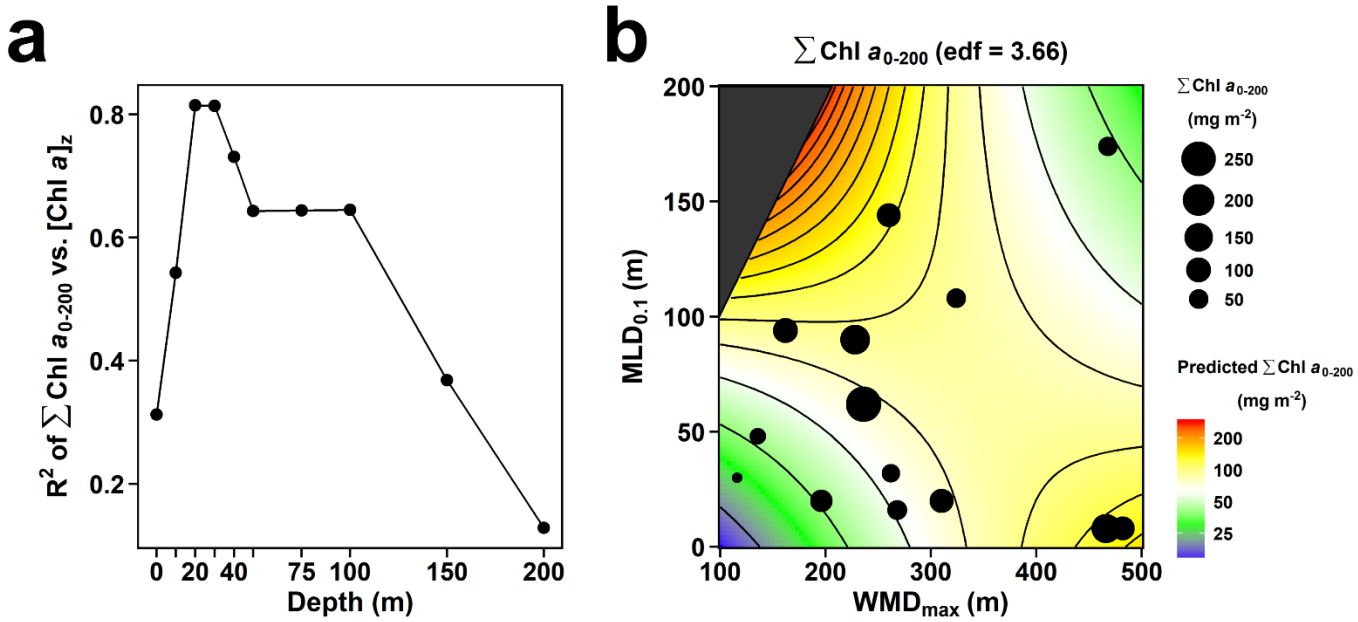

34 **Fig. S1. (a)** Proportion of variance explained (R^2) by the linear regressions between
35 depth-integrated Chl *a* (0-200 m, ΣChl $a_{0\text{-}200}$) and Chl *a* concentration at each sampling
36 depth ([Chl *a*]$_z$) in March. **(b)** Observed (dot size) and predicted (contour plot) ΣChl $a_{0\text{-}200}$ in March. Predicted values were obtained based on a generalized additive model
38 (GAM) that included an interaction term between the maximum winter mixing depth
39 (WMD_{max}) and the near-surface stratification depth in each sampling date ($MLD_{0.1}$). The
40 R^2 for the model was 0.52 and the interaction term had a p-value = 0.209. The estimated
41 degrees of freedom (edf) for the model are indicated. The dark gray triangles on the top
42 left corners delimit those combinations of WMD_{max} and $MLD_{0.1}$ that are not possible
43 (WMD_{max} cannot be shallower than $MLD_{0.1}$). Note that predicted ΣChl $a_{0\text{-}200}$ is shown in
44 $\log_{10}$ scale.

References

Hastie, T. J., and R. J. Tibshirani. 1990. Generalized additive models. Chapman & Hall/CRC.

Kvile, K. Ø., Ø. Langangen, I. Prokopchuk, N. C. Stenseth, and L. C. Stige. 2016. Disentangling the mechanisms behind climate effects on zooplankton. Proc. Natl. Acad. Sci. USA **113:** 1841-1846. doi:10.1073/pnas.1525130113

Murase, H., H. Nagashima, S. Yonezaki, R. Matsukura, and T. Kitakado. 2009. Application of a generalized additive model (GAM) to reveal relationships between environmental factors and distributions of pelagic fish and krill: a case study in Sendai Bay, Japan. ICES J. Mar. Sci. **66:** 1417-1424. doi:10.1093/icesjms/fsp105

Stenseth, N. C., M. Llope, R. Anadón, L. Ciannelli, K. S. Chan, D. Ø. Hjermann, E. Bagøien, and G. Ottersen. 2006. Seasonal plankton dynamics along a cross-shelf gradient. Proceedings of the Royal Society B: Biological Sciences **273:** 2831-2838.

Wood, S. N. 2006. Generalized additive models: an introduction with R. Chapman and Hall/CRC.